Numerical study of Asian dust transport during the springtime of 2001 simulated with the Chemical Weather Forecasting System (CFORS) model

Itsushi Uno,[1] Shinsuke Satake,[1] Gregory R. Carmichael,[2] Youhua Tang,[2] Zifa Wang,[3] Toshihiko Takemura,[1] Nobuo Sugimoto,[4] Atsushi Shimizu,[4] Toshiyuki Murayama,[5] Thomas A. Cahill,[6] Steven Cliff,[6] Mitsuo Uematsu,[7] Sachio Ohta,[8] Patricia K. Quinn,[9] and Timothy S. Bates[9]

Received 6 October 2003; revised 12 April 2004; accepted 26 May 2004; published 14 September 2004.

[1] The regional-scale aerosol transport model Chemical Weather Forecasting System (CFORS) is used for analysis of large-scale dust phenomena during the Asian Pacific Regional Characterization Experiment (ACE-Asia) intensive observation. Dust modeling results are examined with the surface weather reports, satellite-derived dust index (Total Ozone Mapping Spectrometer (TOMS) Aerosol Index (AI)), Mie-scattering lidar observation, and surface aerosol observations. The CFORS dust results are shown to accurately reproduce many of the important observed features. Model analysis shows that the simulated dust vertical loading correlates well with TOMS AI and that the dust loading is transported with the meandering of the synoptic-scale temperature field at the 500-hPa level. Quantitative examination of aerosol optical depth shows that model predictions are within 20% difference of the lidar observations for the major dust episodes. The structure of the ACE-Asia Perfect Dust Storm, which occurred in early April, is clarified with the help of the CFORS model analysis. This storm consisted of two boundary layer components and one elevated dust (>6-km height) feature (resulting from the movement of two large low-pressure systems). Time variation of the CFORS dust fields shows the correct onset timing of the elevated dust for each observation site, but the model results tend to overpredict dust concentrations at lower latitude sites. The horizontal transport flux at 130°E longitude is examined, and the overall dust transport flux at 130°E during March–April is evaluated to be 55 Tg. *INDEX TERMS:* 0305 Atmospheric Composition and Structure: Aerosols and particles (0345, 4801); 0322 Atmospheric Composition and Structure: Constituent sources and sinks; 0368 Atmospheric Composition and Structure: Troposphere—constituent transport and chemistry; 3210 Mathematical Geophysics: Modeling; *KEYWORDS:* Asia, soil dust, simulation, observation, ACE-Asia

Citation: Uno, I., et al. (2004), Numerical study of Asian dust transport during the springtime of 2001 simulated with the Chemical Weather Forecasting System (CFORS) model, *J. Geophys. Res.*, *109*, D19S24, doi:10.1029/2003JD004222.

1. Introduction

[2] There is a strong interannual variability in the occurrence of Asian dust events. A remarkable number of dust storms were reported during 2000–2002. Total dust emission quantities over the Asian region are estimated to be 100–200 Tg. This amount corresponds to approximately 10% of total annual global dust emission [*Intergovernmental Panel on Climate Change* (*IPCC*), 2001]. However, Asian dust has a very clear seasonal cycle, with most of the dust erosion over the Gobi desert region occurring during the springtime [e.g., *Kurosaki and Mikami*, 2003]. Thereby, spring dust storms and yellow sand (kosa) exert an important impact on Asian air quality. Moreover, interactions between dust and pollution is an important issue of the Asian atmospheric environment and the aerosol-laden air helps to modulate atmospheric radiation [e.g., *Nakajima et al.*, 2003]. Radiation effects of

[1]Research Institute for Applied Mechanics, Kyushu University, Kasuga, Japan.
[2]Center for Global and Regional Environmental Research, University of Iowa, Iowa City, Iowa, USA.
[3]Institute of Atmospheric Physics, Chinese Academy of Sciences, Beijing, China.
[4]National Institute for Environmental Studies, Tsukuba, Japan.
[5]Tokyo University of Marine Science and Technology, Tokyo, Japan.
[6]DELTA Group, Chemical Engineering, University of California, Davis, California, USA.
[7]Ocean Research Institute, University of Tokyo, Tokyo, Japan.
[8]Faculty of Engineering, Hokkaido University, Sapporo, Japan.
[9]NOAA Pacific Marine Environmental Laboratory, Seattle, Washington, USA.

0148-0227/04/2003JD004222$09.00

mineral dust have also been studied using global models [e.g., *Takemura et al.*, 2000].

[3] The IGAC/IGBP Asian Pacific Regional Aerosol Characterization Experiment (ACE-Asia) intensive observation [*Huebert et al.*, 2003] was conducted to facilitate a better understanding of Asian aerosols for air quality and their impact on the radiation budget. Ace-Asia provided an excellent observational data set to help elucidate Asian dust transport and radiation impacts. Several modeling activities for the radiation budget were reported by *Nakajima et al.* [2003] based on global aerosol chemical transport model (CTM) and *Conant et al.* [2003] by regional aerosol CTM. *Tang et al.* [2004] recently reported the 3-D distribution of aerosol and its interaction with atmospheric chemistry. The 3-D characteristics of aerosols over Asia were also described on the basis of the regional-scale CFORS model output [*Uno et al.*, 2003a; *Satake et al.*, 2004]. *Chin et al.* [2003] specifically addressed forecasting performance of 3-D global aerosol model, GOCART, during the ACE-Asia studies.

[4] Recent advances in dust modeling focused on the ACE-Asia experiment have been reported by *Gong et al.* [2003] and *Liu et al.* [2003]. *Gong et al.* [2003] applied the Northern Aerosol Regional Climate Model (NARCM) with 45 km resolution over China to northwestern Canada with a sophisticated dust emission/transport model. They estimated that ~250 Mt (Tg) of soil dust below $d < 40$ μm was emitted during March to May. *Liu et al.* [2003] applied a high-resolution regional dust model with 27 km grid for the period of 1–16 April 2001, and estimated emissions of 640 Tg of soil below $d < 36$ μm. Although these total dust emissions are quite different, they produced good model performance when compared with surface aerosol observations and lidar data, and this indicates that more quantitative evaluation between dust model and observation data are required.

[5] Several dust-modeling studies in different years have also been reported. *Park and In* [2003] applied their regional dust model for spring 2002. They estimated 480 Tg of soil dust ($d < 70$ μm) during 19–23 March 2002. *Shao et al.* [2002] applied their global dust model over Asia with a detailed dust scheme including saltation bombardment. They reported an averaged dust flux of 4.6 Tg/day ($d < 22$ μm) during the dust episode of 6–10 April 2002. This wide scatter of estimated dust emission reflects differences in the dust emission schemes, surface boundary data (such as land use, soil texture, soil wetness), and dust transport model. More detailed studies are required to reduce the uncertainties in Asian dust emission and transport. *Nickovic et al.* [2001] have shown the importance of detailed dust modeling for Sahara dust regions.

[6] ACE-Asia produced a comprehensive dust/aerosol observation data set. Detailed analyses comparing surface aerosol observation data, lidar observation data, synoptic-scale weather conditions, and the 3-D structure of huge dust storms during the ACE-Asia studies are necessary to develop a quantitative assessment of the performance of the current regional-scale dust/aerosol transport models. The purposes of this paper are as follows: (1) to provide a detailed analysis of dust emission/transport/structure, (2) to quantitatively assess the dust simulation results from springtime 2001 on the basis of the Chemical Weather Forecasting System (CFORS) model [*Uno et al.*, 2003a] and ACE-Asia observation data, and (3) to identify the key parameters needed to establish more detailed and quantitative dust models. The structure of this paper is as follows. Section 2 describes briefly the CFORS dust modules. Section 3 shows Global Telecommunication System (GTS) synoptic weather report (SYNOP) data and lidar measurement data at Beijing [*Shimizu et al.*, 2004], and identifies the three major dust episodes for detailed analysis in this paper. In section 4.1 the analysis of the relationship among the 500 hPa temperature field, the modeled vertical column dust loading and Total Ozone Mapping Spectrometer (TOMS) Aerosol Index (AI) for the dust storm transport is presented. Section 4.2 presents a detailed comparison with Mie-scattering lidar data and describes the 3-D dust structure. Section 4.3 provides a detailed structural 3-D description of ACE-Asia Perfect Dust Storm (PDS) that occurred in early April 2001. Section 4.4 shows a comparison with surface trace metal observations, and section 4.5 summarizes the dust transport flux at 130°E longitude. Finally, the conclusions are summarized in section 5.

2. CFORS Dust Module Description

[7] CFORS [*Uno et al.*, 2003a] is designed as a multi-tracer, online system built within the Regional Atmospheric Modeling System (RAMS) [*Pielke et al.*, 1992; *Cotton et al.*, 2003]. A unique feature of CFORS is that multiple tracers are run online in RAMS, so that all the meteorological information from RAMS is used directly by the tracer model at every time step (~90 s). Tracers used in CFORS are both anthropogenic species (SO_2/SO_4, CO, black carbon (BC), organic carbon (OC), fast and slow reacting hydrocarbons) and natural origin species (mineral dust, sea salt, radon (Rn), volcanic SO_2). Both the aerosol extinction coefficient and single scattering albedo (SSA) were calculated for comparison with observation data [*Satake et al.*, 2004; *Takemura et al.*, 2000].

[8] The CFORS system treats size-resolved mineral dust using 12 particle size bins. The 12 size ranges are 0.1–0.16, 0.16–0.25, 0.25–0.40, 0.40–0.63, 0.63–1.00, 1.00–1.58, 1.58–2.51, 2.51–3.98, 3.98–6.31, 6.31–10.0, 10.0–15.85, and 15.85–25.12 μm in radius, with corresponding effective radii of 0.13, 0.21, 0.33, 0.52, 0.82, 1.27, 2.01, 3.19, 4.06, 8.01, 12.7, and 20.1 μm, respectively. Mineral aerosols are emitted into the atmosphere by high-velocity surface winds. In CFORS, the total dust uplift flux, F_{dust} ($kg/m^2/s$), is calculated online using a fourth-power law function of surface friction velocity u_* [*Gillette and Passi*, 1988]. The initial dust uplift height (i.e., the injection height) is very uncertain. In the CFORS dust module, the mixing height Z_{BL} is diagnosed from the vertical potential temperature profile (from RAMS); the uplifted dust mass-mixing ratio is distributed uniformly within the Z_{BL}. Within CFORS, natural dust emission areas are defined as desert and semi-desert areas from the data set of 1-km resolution land cover characteristics produced by the U.S. Geological Survey (USGS) (based on AVHRR data obtained in 1992–1993).

[9] Results from more sophisticated emission schemes [e.g., *Nickovic et al.*, 2001; *Gong et al.*, 2003; *Zender et al.*, 2003; *Shao et al.*, 2002] have been reported; however, such dust models require large amounts of detailed information on soil texture, dust and sand size distribution, threshold

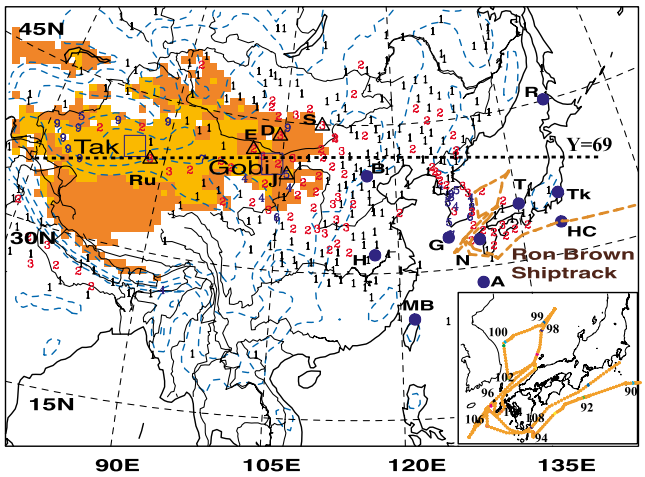

Figure 1. The main part of the CFORS model domain (the subdomain of x grids from 1 to 90 and y grids from 30 to 90 are shown). Trace metal and lidar observations are shown with solid blue circles. Dust observation number at the SYNOP networks during March–April 2001 is shown. Brown dashed line is the *Ron Brown* ship track. Line at $Y = 69$ is used in the Figure 9 vertical section. The brown region is the desert and semidesert region, and the blue dashed lines are the elevation level.

velocity for dust lift-up, and the effect of soil wetness, some of which are difficult to determine over inland China areas. This paper specifically examines performance of the relatively simple CFORS dust emission schemes.

[10] Figure 1 shows the model domain. The numerical model domain of CFORS is centered at 25°N 115°E on a rotated polar stereographic system. The horizontal grid comprises 100 by 90 grid points with a resolution of 80 km (Figure 1 shows the subdomain of x grids from 1 to 90 and y grids from 30 to 90). The model's vertical domain extends from the surface to 23 km with 22 stretching grid layers varying from 150 m thick at the surface to 1800 m thick at the top. This model domain can simulate long-range transport of mineral dust both from Taklimakan and the Gobi desert regions. In Figure 1, solid circles indicate lidar and surface aerosol observation sites (described in section 4), open triangles are the SYNOP observation sites used in Figure 2, and the numbers are dust observation count (total number of date when the dust phenomena were reported) during March and April 2001 (total observation count is divided by 10). The brown dashed line indicates the ship track of the NOAA research vessel *Ron Brown* [*Bates et al.*, 2004]. The straight dashed line shows the selected west-east cross section at the $Y = 69$ grid for the dust transport analysis used in section 4.2.

[11] RAMS/CFORS is a regional meteorological model that requires initial and boundary meteorological conditions. For long-term simulations, a four-dimensional data analysis (FDDA) option using the nudging technique was included on the basis of RAMS/Isentropic Analysis Package (ISAN) output. In this paper, the ECMWF reanalysis data, with 1° × 1° resolution (6 hour interval at specified pressure levels of 1000, 925, 850, 700, 500, 400, 300, 250, 200, 150, 100, 70, 50, 30, and 10 hPa) for the ISAN processor input. CFORS was applied for the period of 20 February to 31 May 2001 with weekly SST data; we also used observed monthly snow cover data. More details of CFORS are described by *Uno et al.* [2003a] and *Satake et al.* [2004].

3. Selection of the Major Dust Episodes

[12] During spring 2001 numerous dust episodes were observed [e.g., *Gong et al.*, 2003; *Kurosaki and Mikami*, 2003]. Many of them were observed within the ACE-Asia intensive observation networks. The CFORS model simulation period covered most of the dust episodes. However, a complete analysis of dust episodes during spring 2001 is not the main objective of this paper. This paper restricts the analysis period on the basis of surface dust reports and Mie-scattering lidar measurement at Beijing.

[13] Figure 2 shows the time variation of the observed surface wind speed (open circles) and weather code at five locations (Ruoqiang, Ejin Qi, Jartai, Dalanzadgad, and Sajnsand) (dollar signs). Table 1 shows information for those geographical locations.

[14] This study uses six-hour data obtained by conventional surface meteorological observations (SYNOP reports) in east Asia in March and April 2001. These weather data are based on World Meteorological Organization (WMO) observation weather codes (ww). Dollar signs on the 10 m/s wind speed represent that floating dust (ww = 06) was observed, whereas dollar signs at the level of 15 m/s shows a reported dust storm (ww = 07–09 and 31–35). It should be noted that SYNOP weather reports are highly dependent on observers' personal experiences and on the spatial distribution of the observation sites. The difference between nighttime and daytime observations also affects observers' judgments. Surface weather stations cannot provide quantitative information on mass loading associated with dust storms. Notwithstanding this, they comprise a valuable data set on the occurrence and the temporal and spatial characteristics of the large-scale dust features that can be compared with model results (e.g., reported surface visibility). Figure 1 shows that the number of dust reports in the Gobi, Inner Mongolia of China, Mongolia exceeded 30. The western edge of the Tarim basin station reported more than 90 dust reports. In Korea and the western side of Japan, dust reports exceeded 20 counts (mainly floating dust).

[15] Accurate prediction of the surface wind speed is critical for dust modeling. Figure 2 also shows the RAMS/CFORS wind speed at 10 m height with black lines and the simulated dust concentration averaged from surface to 400 m height with red-shaded lines. The model elevation is averaged over 80 km regions. For that reason, it does not agree with the actual elevation at observation sites, and the modeled wind speed does not agree completely with the observations. However, it is shown that the time variation of modeled wind speed captured the main peaks of the strong winds. When compared with the dust reports and model dust concentrations, the CFORS dust simulation is able to reproduce the major observed dust episodes. This is especially so for Julian days (hereinafter Jday) 61–66 (2–7 March) at Jartai and Dalanzadgad, 72–75 (13–16 March) at Ruoqiang, 77–84 (18–25 March) at Jartai, and 93–102 (3–12 April) at all five sites. CFORS results also reproduced dust storms during Jdays 112–116 (22–26 April) at Ejin Qi and Jartai.

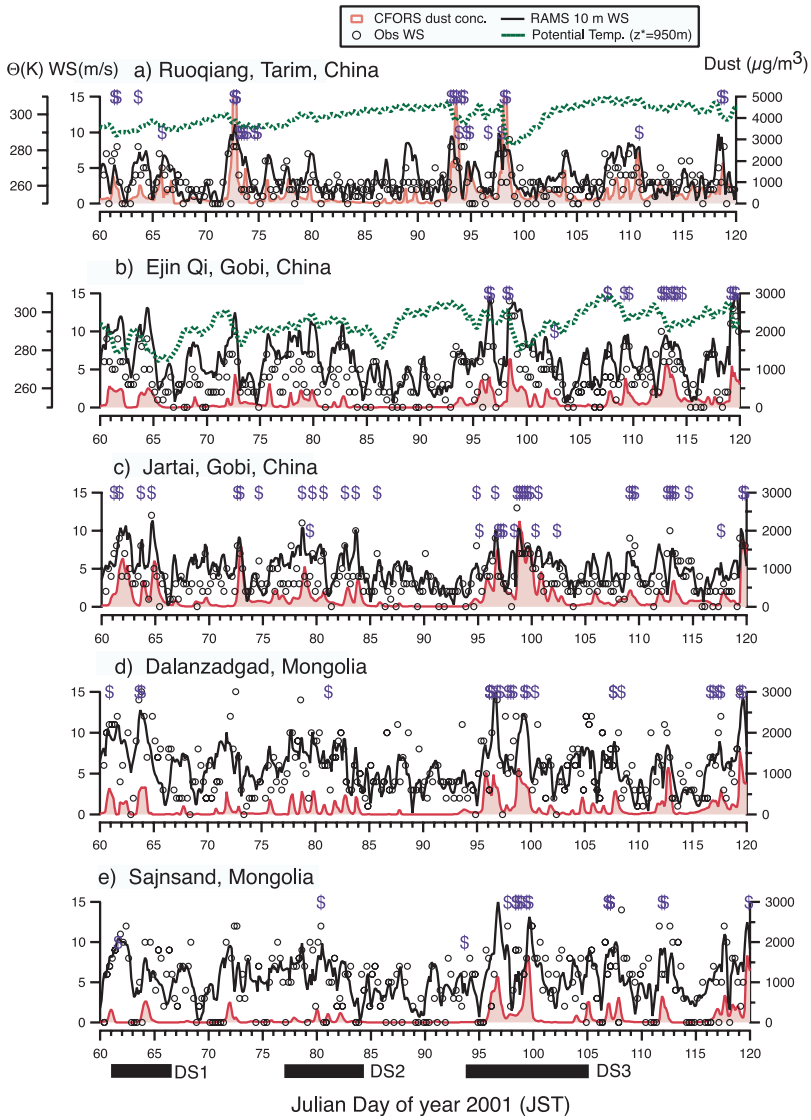

Figure 2. (a–e) Time series variation of SYNOP surface wind speed (open circles) and dust report (dollar signs). The black line is CFORS model wind speed at 10 m height; the red line is CFORS dust concentration. Green lines in Figures 2a and 2b show potential temperature at z = 950 m.

[16] Figures 2a and 2b show the time variation of the potential temperature (at z = 950 m above topography) with green lines. Potential temperatures are averaged within a nine-grid area as shown in Figure 1 (as identified Tak and Gobi and the averaged elevation in the model is 1013 m and 1274 m, respectively). Large potential temperature drops are positively correlated with high wind speed and increasing dust concentration. This positive correlation between potential temperature drop and dust concentration indicates that the dust emission is triggered by cold front activities.

[17] Figure 3a shows the observed dust extinction coefficient by the continuous polarization Mie-scattering lidar system [*Shimizu et al.*, 2004]. The lidar measurement method will be discussed in section 5.1. The white areas during Jdays 68–74 and 96–101 are undefined because the boundary layer aerosol concentration was so dense that the lidar signal could not penetrate into the upper layer. Figure 3e shows Aerosol Robotic Network (AERONET) daily observation of aerosol optical depth (AOD) and the Ångstrom exponent, alpha. AERONET observations started from Jday 66. We will describe Figure 3 fully in section 5.

[18] Figure 3a shows that at least seven dust episodes were observed in Beijing during this period. These were Jdays 61–66, Jdays 68–74, Jdays 78–84, Jdays 92–95, Jdays 97–102, Jdays 107–113 and Jdays 118–121. During these episodes, the AERONET alpha value were below 0.5 during Jdays 78–84, Jdays 97–100, and Jdays 104–106. During Jdays 68–74 and Jdays 92–95, alpha was relatively high, reflecting the effects of local air pollution as observed by the lidar signals on those days. Alpha values for Jdays 61–66 were not observed. However, the TOMS Aerosol Index (AI) was high during this period [*Satake et al.*, 2004] over the Beijing area, and TOMS AI is sensitive to mineral dust. The dust signals during Jdays 61–66 also represent large-scale dust transport.

[19] On the basis of these considerations we selected three major dust episodes for detailed analysis; they are DS1 (Jdays 61–66), DS2 (Jdays 77–84), and DS3 (Jdays

Table 1. Location of Observation Stations

Station[a]	Period, Julian days	Longitude, °E	Latitude, °N	Elevation ASL, m	Measured Items Used in This Paper[b]	Remarks
GTS SYNOP station						
Ruoqiang, China (Ru)	March and April 2001 (routine)	88.17	39.03	889	1	SYNOP station code 51777
Ejin Qi, China (E)	March and April 2001 (routine)	101.07	41.95	941	1	SYNOP station code 52267
Jartai, China (J)	March and April 2001 (routine)	105.75	39.78	1033	1	SYNOP station code 53502
Sajnsand, Mongolia (S)	March and April 2001 (routine)	110.12	44.90	936	1	SYNOP station code 44354
Dalanzadgad, Mongolia (D)	March and April 2001 (routine)	104.42	43.58	1465	1	SYNOP station code 44373
Mie-scattering lidar						
Beijing, China (B)	March and April 2001	116.28	39.93	55	2	*Shimizu et al.* [2004]
Nagasaki, Japan (N)	March and April 2001	129.86	32.78	30	2	*Shimizu et al.* [2004]
Tsukuba, Japan (Tk)	March and April 2001	140.12	36.05	20	2	*Shimizu et al.* [2004]
DELTA Group site						
Beijing, China (B)	80–115	116.28	39.93	55	3	*Cahill et al.* [2002]
Gosan, Korea (G)	82–119	126.16	33.29	78	3	*Cahill et al.* [2002]
Mount Bamboo, Taiwan (MB)	76–106	121.56	25.21	827	3	*Cahill et al.* [2002]
Hefei, China (H)	82–125	117.16	31.90	60	3	*Cahill et al.* [2002]
Tango, Japan (T)	79–108	135.17	35.70	600	3	*Cahill et al.* [2002]
VMAP site						
Rishiri, Japan (R)	April 2001	141.20	45.12	35	4	*Matsumoto et al.* [2003]
Hachijo, Japan (Hc)	April 2001	139.75	33.15	80	4	*Matsumoto et al.* [2003]
APEX site, Amami-Oshima, Japan (A)	92–119	129.70	28.44	15	5	*Nakajima et al.* [2003]
NOAA research vessel *Ron Brown*	75–109 (90–109 Japan Area)	see Figure 1	see Figure 1	18	6	*Bates et al.* [2004] and *Quinn et al.* [2004]

[a]Symbols in parentheses are plotted in Figure 1.
[b]Measured items used in this paper: 1, wind speed, wind direction, pressure, precipitation, temperature, visibility, current weather; 2, backscattering coefficient, extinction coefficient (separated from dust and nondust by depolarization ratio); 3, Al, S, Ca (0.09–0.26, 0.26–0.34, 0.34–0.56, 0.56–0.75, 0.75–1.15, 1.15–2.5, 2.5–5.0, and 5.0 to ~12.5 μm); 4, Al, SO_4, Ca (d < 2.5 μm and total); 5, Al, SO_4 (d < 2.0 μm and total); 6, Al, SO_4, Ca, AOD (submicron and sub-10 μm sample).

94–104). These periods are shown by thick horizontal bar in Figures 2 and 3. These major dust episodes are consistent with the ones reported by *Gong et al.* [2003]. Similarly, *Liu et al.* [2003] targeted the large-scale dust episode covering the DS3 period with very high-resolution dust transport model. The DS3 includes the period of the ACE-Asia "Perfect Dust Storm (PDS)" episode.

[20] Dust storms were observed both in the Taklimakan and Gobi deserts in DS1 and DS3; in DS2, only the Gobi region reported dusty weather. Potential temperature levels between Taklimakan and Gobi region (shown in Figures 2a and 2b) differ during DS1. That is, the potential temperature level in the Gobi was colder (by about 10 K) than that in the Taklimakan. Potential temperature within the specific air mass can be considered as a preserved quantity during transport, so a primary conclusion of the origin of DS1 dust in Beijing is that it comes from the Gobi region. During DS3 the potential temperature levels were almost equal over the Gobi and Taklimakan regions (about 294–298 K in Jdays 94–96, and 285 K in Jdays 98–100); therefore more detailed analysis using model results is necessary to determine the origin and transport processes of the dust.

4. Results and Discussion

[21] In this section we first show the analysis of the relationship among the 500 hPa temperature field, the modeled vertical column dust loading and TOMS Aerosol Index (AI) for the dust storm transport. Then a detailed comparison with Mie-scattering lidar data that helps describe the 3-D dust structure is presented. Detailed 3-D structure of ACE-Asia Perfect Dust Storm (PDS) that occurred in early April 2001 is then presented and compared with surface trace metal observations. Finally, dust transport fluxes are estimated.

4.1. Horizontal Transport of the Major Dust Episodes: Dust Loading, 500-hPa Temperature, TOMS AI, and Daily Dust Signal

[22] This section examines the horizontal dust transport process during the three major dust episodes selected in section 3. Large-scale synoptic meteorological analysis based on a 500 hPa temperature field from RAMS output is used because the cold air trough can be seen clearly at the 500 hPa level. The vertical dust loading (column dust concentration) from CFORS simulation and the TOMS Aerosol Index (AI) are also used in the analysis. TOMS AI can capture aerosol information at the top of the cloud layer, but information below the cloud is unobtainable. Notwithstanding, it provides useful information regarding horizontal dust distribution. It is also important to note that elevated TOMS AI values are not unique to dust. Hazy weather caused by biomass combustion also results in the high AI value, and this is important in southern Asia.

[23] Figures 4–6 show the 500 hPa temperature (purple dashed lines), modeled column loading of dust (blue solid line), TOMS Aerosol Index (color), and the SYNOP dust weather report for DS1, DS2, and DS3 dust episodes,

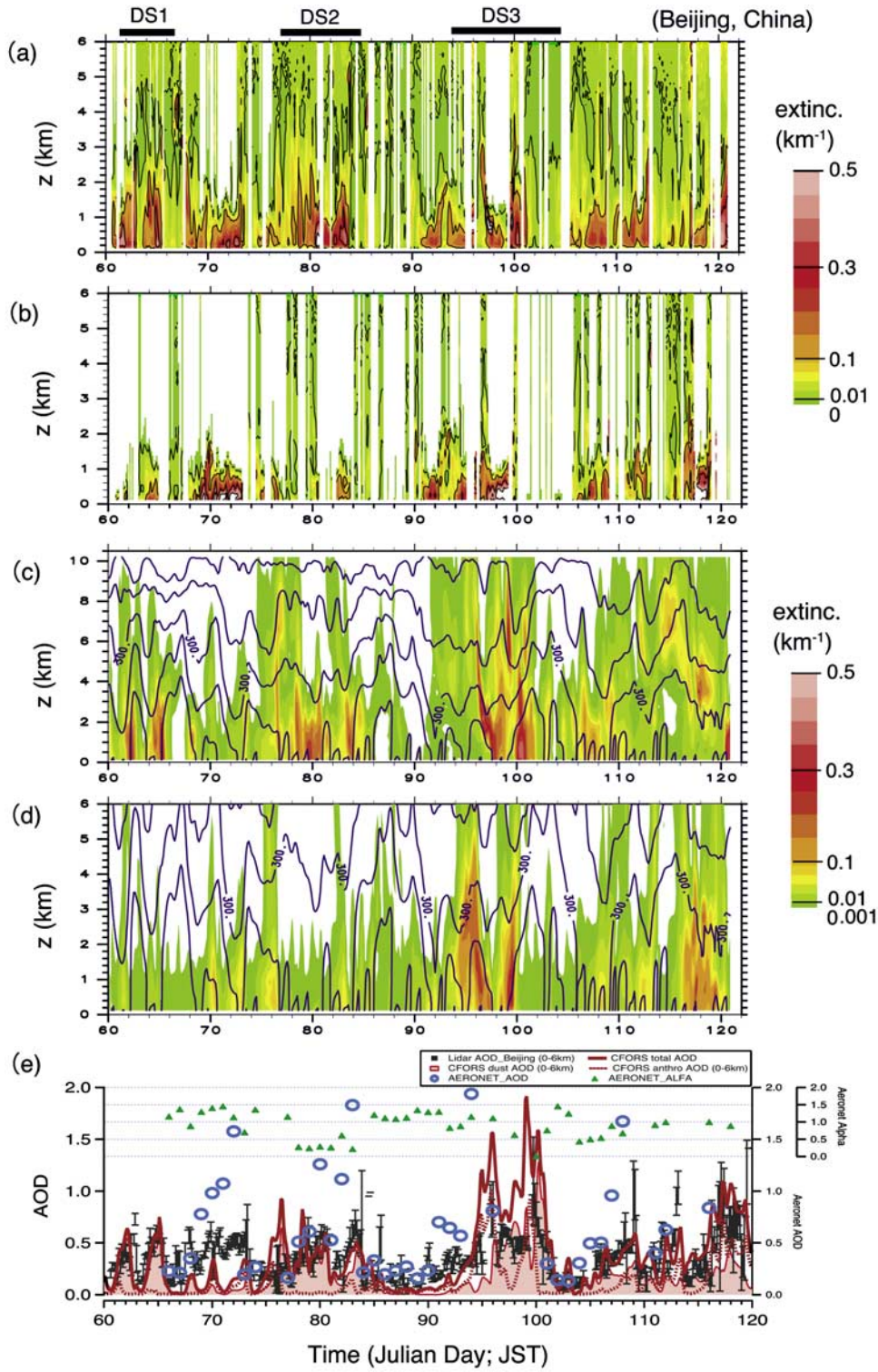

Figure 3. Observed and CFORS results for Beijing: (a) lidar extinction coefficient for dust; (b) lidar extinction coefficient for nondust (air pollution); (c) CFORS dust extinction coefficient (color) with potential temperature (lines with 10 K interval); (d) CFORS sulfate extinction coefficient (color) with potential temperature (lines with 10 K interval); (e) lidar- (black dot with bar range) and CFORS-derived aerosol optical depth (total AOD shown with thick red line; dust from surface to 6 km shown with red line with shading, nondust from surface to 6 km shown with the red dotted line). The open blue circles are AERONET AOD, and the green triangles are AERONET Ångstrom exponent.

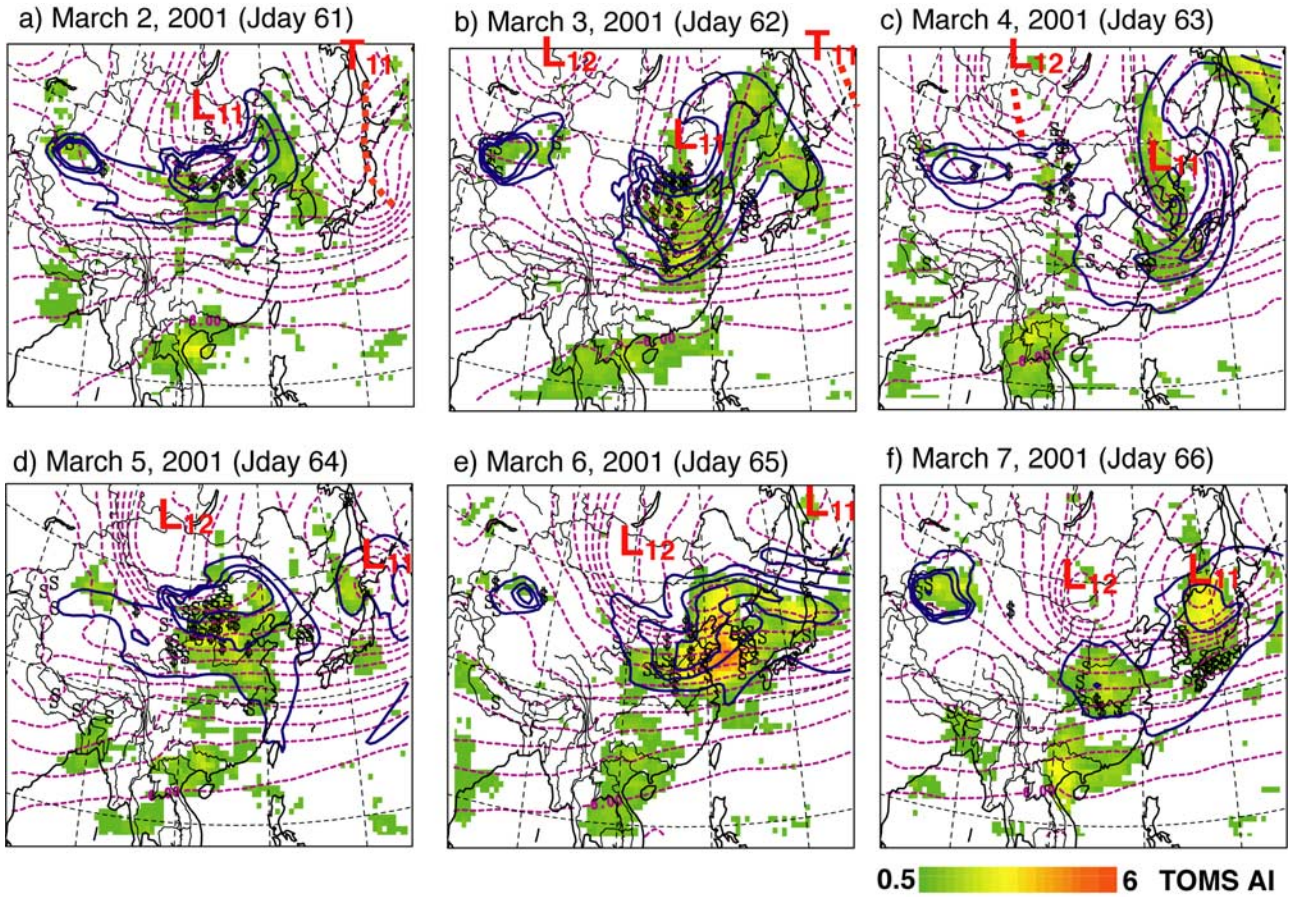

Figure 4. (a–f) Synoptic-scale analysis during the dust episode DS1 of 500 hPa temperature (3°C interval shown with purple dashed lines, vertical column dust loading shown with blue lines, and TOMS Aerosol Index shown with color). The dollar signs indicate stations where the current weather is dusty.

respectively. Dollar signs indicate the locations where surface dust phenomena were observed during the 0000 and 0600 UTC (0900–1500 JST) of respective days. Note that Korea has many SYNOP stations, but that we only selected five stations to show a clear plot of dust reports. In these figures, L_{xy} is the major low-pressure trough, and T_{xy} is the major temperature trough during each episode (where x denotes the index of dust episode and y is the sequential number in each episode).

[24] The predicted CFORS dust loading shows good correlation with TOMS AI. Furthermore, the dust loading movement is correlated with the synoptic-scale meandering (wavy motion) of the 500 hPa temperature field. The dollar symbols generally are seen at the east side of the cold trough (related to the cold front at the surface level) and the main body of the dust loading is transported in the NE direction within the warm sector of the 500 hPa temperature.

[25] Now we specifically address the DS 1 episode (see Figure 4). During this period two low-pressure systems (L_{11} and L_{12}) passed sequentially through the Gobi desert region. The first low hit during Jdays 61–62 (2–3 March) and then traveled eastward to the center of the Sea of Japan on Jday 63 (4 March); thereupon, it became a cutoff low, which remained over Hokkaido and the Sea of Okhotsk until Jday 66 (7 March). The second appeared on Jday 62 (3 March) at the west of Lake Baikal; it then hit the Gobi during the Jdays 63–64 (4–5 March). The temperature of the second low was colder than the first one. These two lows did not directly hit the Taklimakan region. A clean area (dust free region) is also visible between these two lows. For example, the dust loading on Jday 63 (4 March) over the Beijing region was small, which agrees well with the TOMS AI field. Such a clear slit was observed by the lidar as shown in Figure 3a. These two sequentially developed large low-pressure systems were responsible for the dust episode during the DS1 period. The CFORS model results clearly reproduced the onset of these two sequential dust storms.

[26] During dust episode DS2 (see Figure 5) a low-temperature trough T_{21} and T_{22} (equivalently, L_{22}) passed through China from Jdays 78–80 (19–21 March), as shown in Figure 5 with thick red lines. The passing of T_{22} over the Gobi region caused the dust storm shown in Figure 5c. However, the developed low-pressure system at 500 hPa level was not as strong as that in DS1. One main difference is that the trajectory of the center of the low pressure stayed to the north (above 40°N). At the surface level, two low-pressure systems passed over the Japan area on Jdays 79–80 (20–21 March) and Jdays 81–82 (22–23 March), respectively. The 500 hPa temperature field stayed constant and did not take a large meandering motion. The number of dust reports from the Taklimakan and Gobi was smaller when compared with DS1, but dust was reported over a

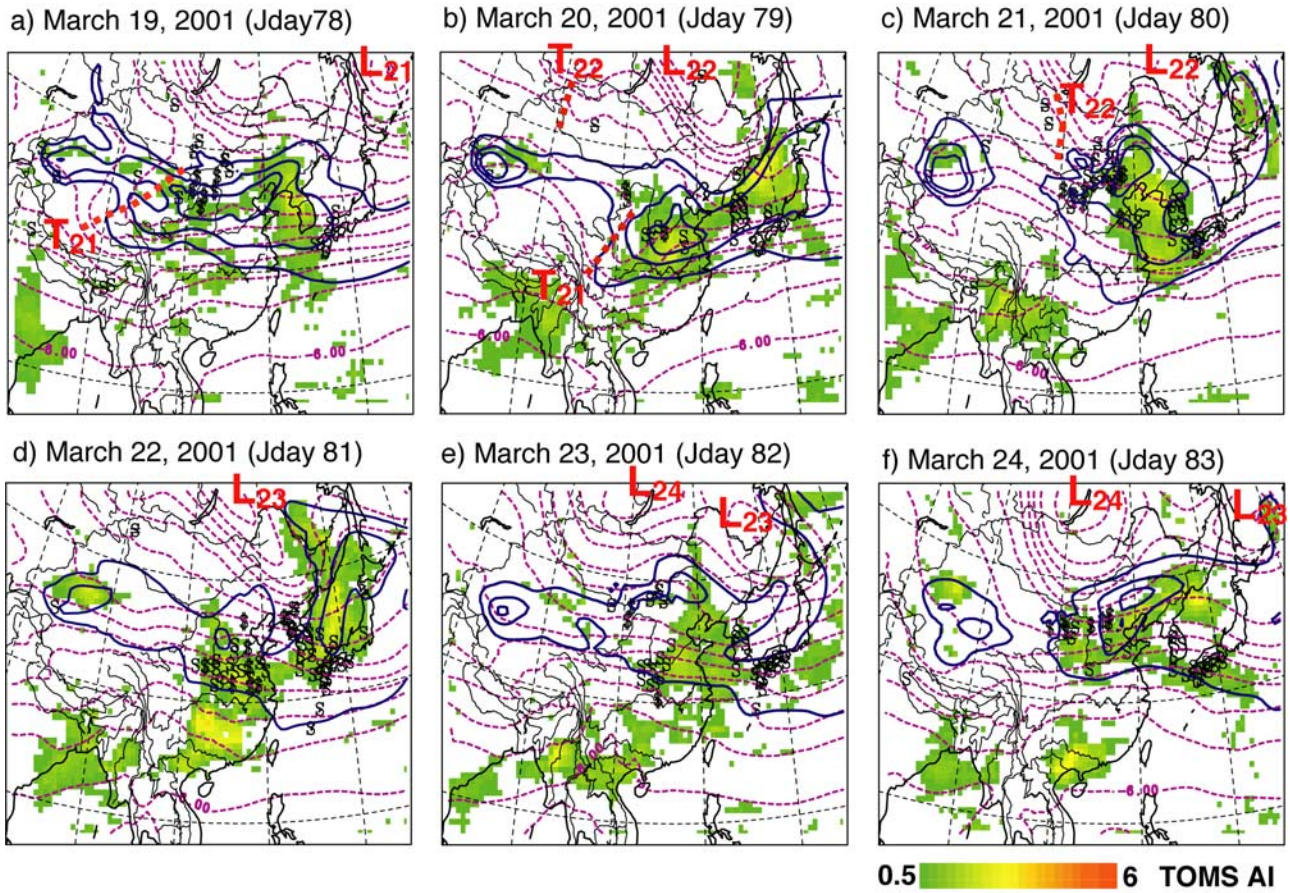

Figure 5. (a–f) Same as Figure 4, except for DS2 (Jday 78–83; 19–24 March 2001).

wide region of western Japan, Korea and the region between the Yellow River and the Yangtze River.

[27] The dust episode in DS3 (see Figure 6) was remarkable. We see two large sequential low-pressure systems (identified as L_{32} and L_{33}) swept over both the Taklimakan and Gobi as in episode DS1, but the scale and strength of the low-pressure system was larger than DS1. Different from the DS1 case, the low-temperature trough hit both the Taklimakan and Gobi regions. A weak temperature trough T_{32} passed through the regions on Jday 94 (4 April), but only slightly dusty conditions were reported in Taklimakan. A developing low of L_{32} appeared on Jday 95 (5 April) over the western edge of the Mongolian boarder, and it arrived over the central part of Mongolia on Jday 96 (6 April). A large number of dust episodes were reported over the Loess Plateau, Inner Mongolia of China and Gobi, and Mongolia. Dust emitted in this episode was transported to the east along the cold front line, and arrived in the region of eastern Mongolia–northeastern China on Jday 97 (7 April). This L_{32} moved to the east at high latitudes ($\sim$40°N) entraining large amounts of dust (Figures 6d and 6e). This dust arrived at Rishiri (R in Figure 1) and Sakhalin on Jday 99–100 (9–10 April). High modeled dust loadings can be seen at the center of L_{32}. Dust from this episode did not affect the south and west parts of Japan.

[28] A second large low, L_{33}, appeared on Jday 97 (7 April) at almost the same location as L_{32}. L_{33} took almost the same route as L_{32} and moved to the east, and it passed over the Taklimakan region on 8 April and the Gobi region on Jday 98–99 (8–9 April). Many dust reports occurred just between L_{32} and L_{33}. On Jday 99 (9 April) Beijing was located in a relatively low dust loading region. Lidar observations also show this decrease in dust (see Figure 3a). High dust levels in this storm were caused by the arrival of L_{33} to Beijing between Jday 99 (9 April) and 100 (10 April). Thereafter the advection speed of this low and cold front slowed. Dust from this episode divided into two major air masses: one transported to the Rishiri on Jday 101 (11 April), and the second part transported at lower latitudes, reaching the southern part of Japan on Jdays 102–103 (12–13 April). These features are clear in the surface observations, as discussed in section 4.4. Figures 3 and 6 show that the CFORS dust model results captured the observed dust distribution during the DS3 episode. It is important to point out that the second low (L_{33}) was approximately 10°C colder than the first one. Potential temperature at $z^* = 950$ m at Gobi area (Figure 2) during the first trough was 296 K, whereas the second one was 285 K. Therefore it is possible to discriminate between these two air masses on the basis of the difference of potential temperature. Sections 4.2 and 4.3 present such a discussion.

4.2. Time-Height Cross Section of Dust: Comparison of Mie Lidar

[29] Examination of the time-height concentration (TH plot of dust) is important for understanding dust transport.

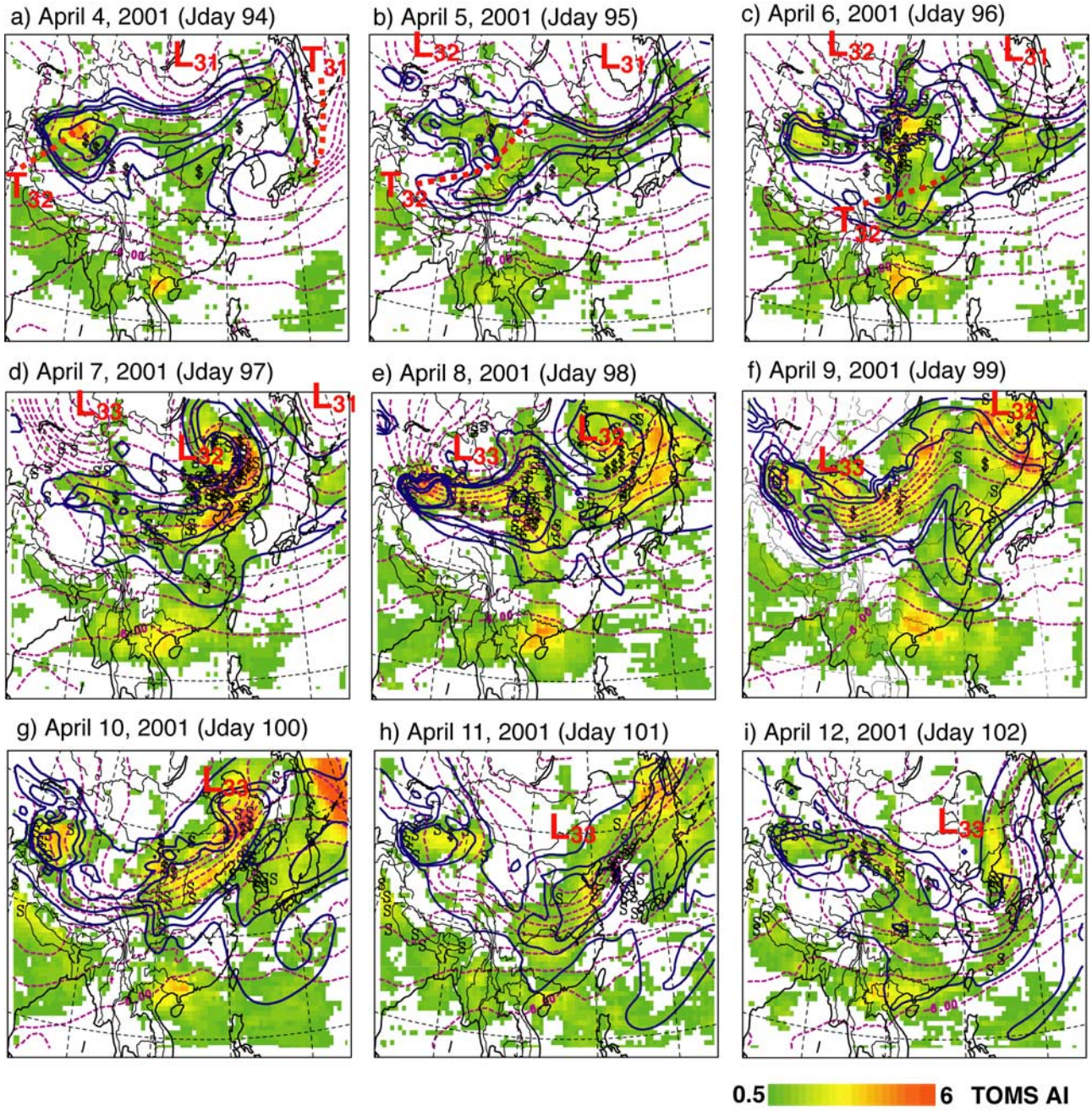

Figure 6. (a–i) Same as Figure 5, except for DS3 (Jday 94–102; 4–12 April 2001).

Some basic comparisons between observations and models have been reported by *Seinfeld et al.* [2004], *Shimizu et al.* [2004], and *Sugimoto et al.* [2002] for Mie lidar measurements. Here, we examine in more detail the dust structure using data on aerosol extinction and aerosol optical depth (AOD), along with source discrimination by potential temperature.

[30] Important dust time-height data are provided by Mie-scattering lidar [*Shimizu et al.*, 2004]. Atmospheric aerosols at Tsukuba, Nagasaki, and Beijing were continuously monitored with a continuous polarization Mie-scattering lidar system during the ACE-Asia 2001 experiment. Such measurement continuity is essential, especially for Asian dust studies, because the timescale of the phenomena is short (typically several hours to a few days). The vertical observation resolution is 30 m. The LIDAR signals were converted to aerosol extinction intensity by the method proposed by *Fernald* [1984]. In that method, the boundary condition of the calculation of extinction coefficient was set at 6 km. The observed extinction coefficient was split into dust and nondust (air pollution) fractions on the basis of the aerosol depolarization ratio δ. *Shimizu et al.* [2004] assumed a constant depolarization ratio for nonspherical particles (e.g., dust) ($\delta = 0.35$) and for spherical particles (air pollutants) ($\delta = 0.02$). Specification of a constant value of δ is based on statistics of measurements tuned for each station. The splitting method details used in ACE-Asia are described by *Sugimoto et al.* [2002] and *Shimizu et al.* [2004].

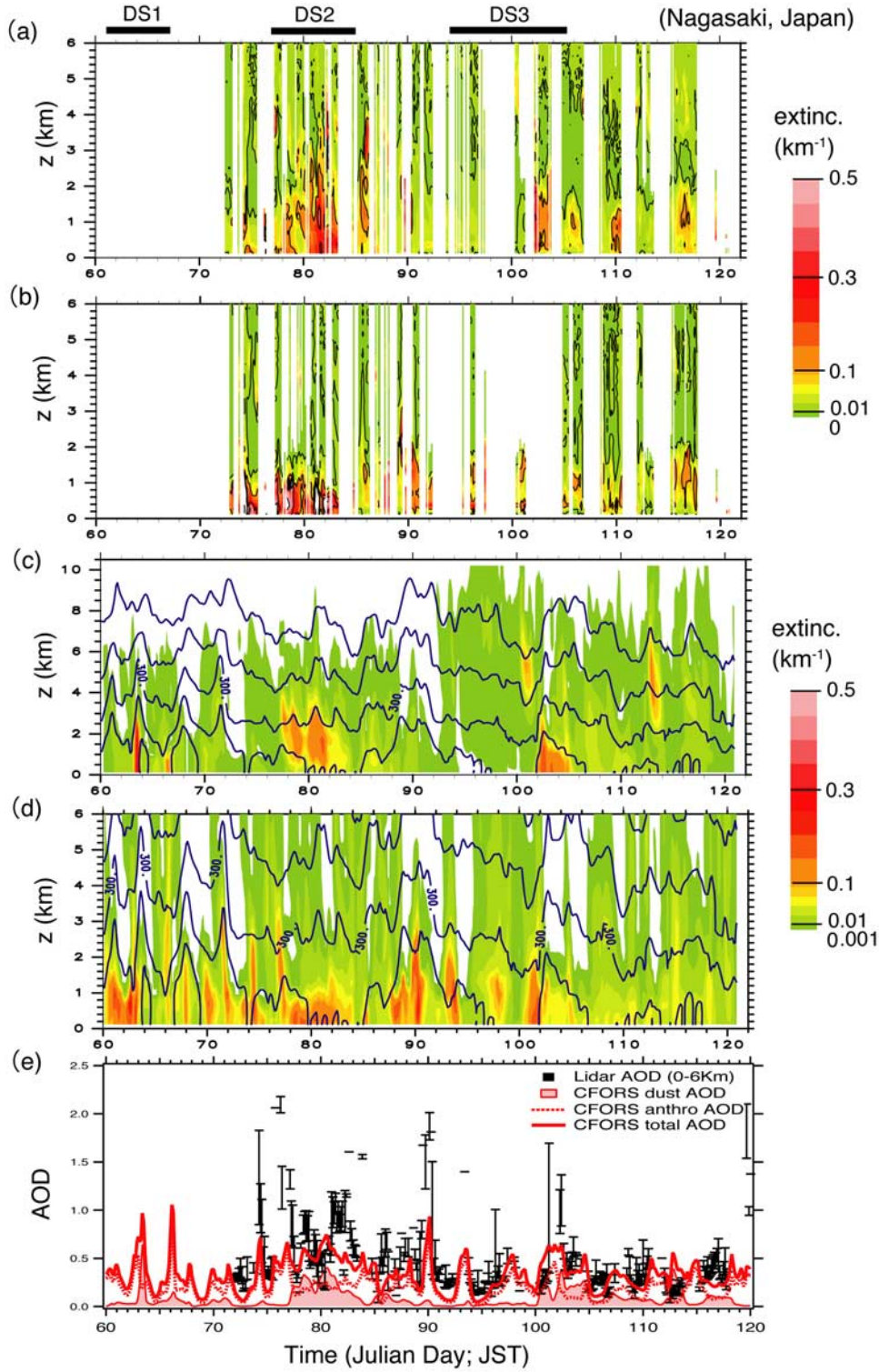

Figure 7. (a–e) Same as Figure 3, but for Nagasaki. The AERONET measurement is not available at Nagasaki.

[31] Figure 3 shows the TH plot of Beijing for observed extinction coefficient for dust by lidar (Figure 3a), observed extinction coefficient for nondust (air pollution) by lidar (Figure 3b), CFORS dust extinction coefficient and potential temperature (Figure 3c), CFORS sulfate extinction coefficient and potential temperature (Figure 3d), and vertically integrated extinction coefficient (from surface to 6 km) for lidar and CFORS (total and dust part), which is equivalent with the AOD between surface to 6 km (Figure 3e). In Figure 3c, the plot continues up to 10-km altitude. In Figure 3e, lidar data are averaged for 3 hours. The vertical bar represents the range of lidar extinction coefficient (maximum and minimum within 3 hours). We also included the AERONET AOD and Ångstrom exponent.

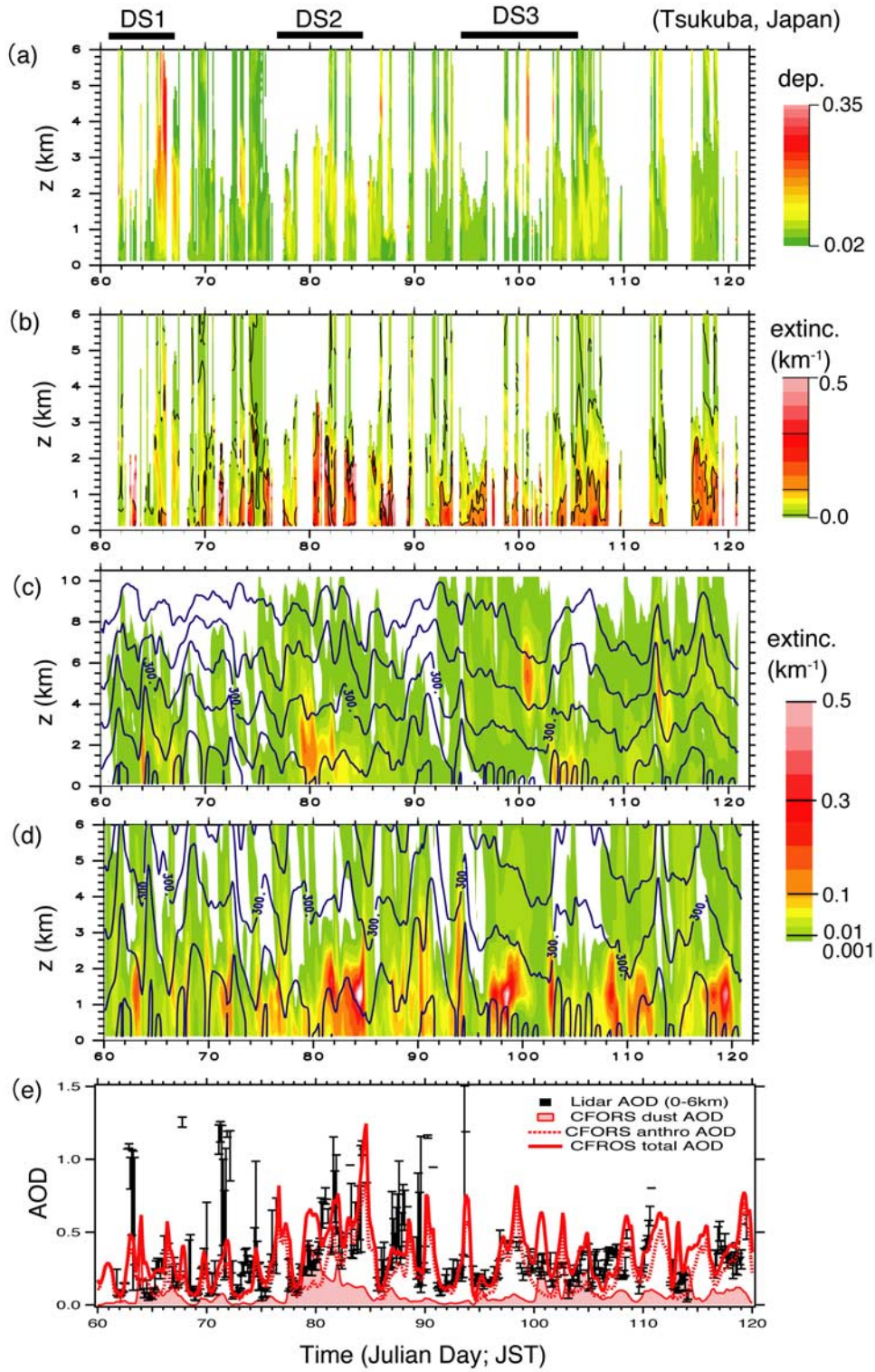

Figure 8. (a–e) Same as Figure 7, but for Tsukuba. Note that Figure 8a shows lidar depolarization ratio, and Figure 8b shows lidar total extinction.

Figure 7 shows identical information to Figure 3 for Nagasaki, Japan. Figure 8 is almost identical to Figure 7, but for Tsukuba, Japan. However, instead of showing the dust and air pollution's extinction coefficient separately, we show depolarization ratio (Figure 8a) and the total extinction coefficient (Figure 8b), This is because δ in Tsukuba is smaller than Nagasaki and Beijing, so the clear separation by use of a single value of δ is difficult and the specification of δ at Tsukuba requires more study.

[32] The CFORS dust fields show good agreement with observed dust profiles for these three sites (Beijing, Nagasaki and Tsukuba). Especially the onset timing and

Table 2. Comparison of Lidar and CFORS Model Aerosol Optical Depth[a]

Station Name	Items	DS-1	DS-2	DS3-1	DS3-2
Beijing	Period, Julian days	61–66	77–84	96–98	99–102
	Lidar [AERONET]	0.36 [-]	0.41 [0.86]	(0.52)[b] [0.81]	0.47 [0.91]
	CFORS-total (6 km)	0.28	0.30	0.82	0.81
	CFORS-dust (6 km)	0.25	0.27	0.54	0.56
	CFORS-nondust (6 km)	0.03	0.03	0.28	0.25
	CFORS-total	0.32	0.36	0.97	1.00
Nagasaki	Period, Julian days	61–66	77–84	96–98	101–104
	Lidar	–	0.70	0.33	0.56
	CFORS-total (6 km)	0.31	0.44	0.26	0.41
	CFORS-dust (6 km)	0.09	0.21	0.03	0.20
	CFORS-nondust (6 km)	0.22	0.23	0.23	0.21
	CFORS-total	0.36	0.52	0.34	0.49
Tsukuba	Period, Julian days	63–66	77–84	96–98	101–104
	Lidar	0.29	0.40	0.31	0.24
	CFORS-total (6 km)	0.23	0.47	0.39	0.25
	CFORS-dust (6 km)	0.07	0.19	0.05	0.12
	CFORS-nondust (6 km)	0.16	0.28	0.34	0.13
	CFORS-total	0.26	0.50	0.44	0.33

[a]Lidar, AOD calculated from lidar total extinction coefficient from surface to 6 km; AERONET, AERONET measurement of AOD shown in brackets; CFORS, AOD calculated from CFORS model. Total (6 km), total AOD from surface to 6 km; dust (6 km), dust AOD from surface to 6 km; nondust (6 km), nondust AOD from surface to 6 km; total, total AOD from surface to the top of model vertical height (22 km).
[b]Vertically averaged below 2 km (lidar measurement was missing above this height).

vertical profiles are well reproduced. Agreement is very good for the three selected dust episodes as DS1, DS2, and DS3. However, the model did not simulate the high dust loadings that occurred near Beijing during the Jdays 68–74 and Jdays 92–94, which are believed to be associated with local Beijing air pollution. It is important to point out that the vertical dimension of the dust layer is trapped in some potential temperature ranges. For example, dust episodes of DS1 at Beijing are restricted to the potential temperatures between 280 K and 290 K and between 290 K and 300 K for DS2. For DS3, the first peak is observed between 290 K and 300 K, whereas the second peak was mainly below 290 K. These potential temperature levels are consistent with the Figures 2a and 3b.

[33] Quantitative comparisons between lidar observation and the CFORS model are shown in Table 2. It includes lidar AOD and CFORS AOD (total, dust and nondust fraction) below 6 km level averaged for each dust episode of DS1, DS2, and DS3. We restricted our comparison periods for DS1, DS2, and DS3 on the basis of the discussion in section 3. Lidar observations, which have missing data, are excluded from this table. In Table 2, DS3 is divided into two parts as DS3-1 (PDS-1) and DS3-2 (PDS-2).

[34] Comparison of Beijing for the DS1 and DS2 periods show excellent agreement between lidar and CFORS predictions. The dust fraction of total AOD exceeded 90%. The lidar measurements at Beijing for DS3-1 are limited because of the overly dense dust layer. For DS3-2, CFORS AOD below 6 km is 70% higher than lidar measurement, but it shows good agreement with AERONET AOD.

[35] The lidar inversion at Nagasaki and Tsukuba is sometimes not performed because of the high frequency of cloud cover. Agreement between modeled and observed time height variation is good for Nagasaki for dust and air pollution. The CFORS model AOD is consistent with lidar AOD for DS2 and DS3. The air pollution fraction in Nagasaki exceeded 50% (in sharp contrast to that of Beijing). Tsukuba shows similar agreement with that of Nagasaki. The fraction of air pollution in Tsukuba is remarkably higher compared with Nagasaki and Beijing. Several reasons exist for this high fraction of air pollution. As discussed in section 4.4, the sulfate level ranges 0–20 $\mu g/m^3$ and shows no big scatter in maximum concentration. Sulfate is a hygroscopic aerosol. Its diameter is a function of relative humidity and very sensitive to calculation of the extinction coefficient. Relative humidity in coastal regions such as Nagasaki and Tokyo is higher than Beijing. Furthermore, the Tokyo area received a strong impact from continuous emissions of SO_2 from the Mount Miyakejima volcano [e.g., *Fujita et al.*, 2003]. These emissions contribute significantly to the high AOD fraction of air pollution in Nagasaki and Tsukuba.

[36] Potential temperature ranges for DS1, DS2, and DS3 at Nagasaki and Tsukuba are similar (see Figures 7b and 8b). These ranges are consistent with that of Beijing. However, the elevation of potential temperature range is slightly higher in Nagasaki (than Beijing). The simulated phenomenon whereby dust is trapped within a specified potential temperature range provides important information for tracking the dust source and path.

[37] Elevated dust layers are found at 4–6 km on Jday 101 (11 April) and 3–6 km on Jday 113 (23 April) in Nagasaki and Tsukuba. *Liu et al.* [2003] also successfully simulated the elevated dust layer over Tsukuba. The CFORS results are quite consistent with those, but the CFORS concentration level is approximately 210 $\mu g/m^3$, whereas it exceeds 1.6 mg/m^3 in the paper by *Liu et al.* [2003]. In general, the calculated AOD levels by the model are consistent (within an average difference of 20%) with lidar measurements when the lidar signals were taken up to 6 km height (excluding DS3 at Beijing and DS2 in the Nagasaki case).

4.3. Structure of the Perfect Dust Storm (PDS)

[38] The dust transport during the DS3 is both complicated and important for understanding the ACE-Asia dust episodes. The CFORS model simulation provides a four-dimensional representation of dust and meteorological

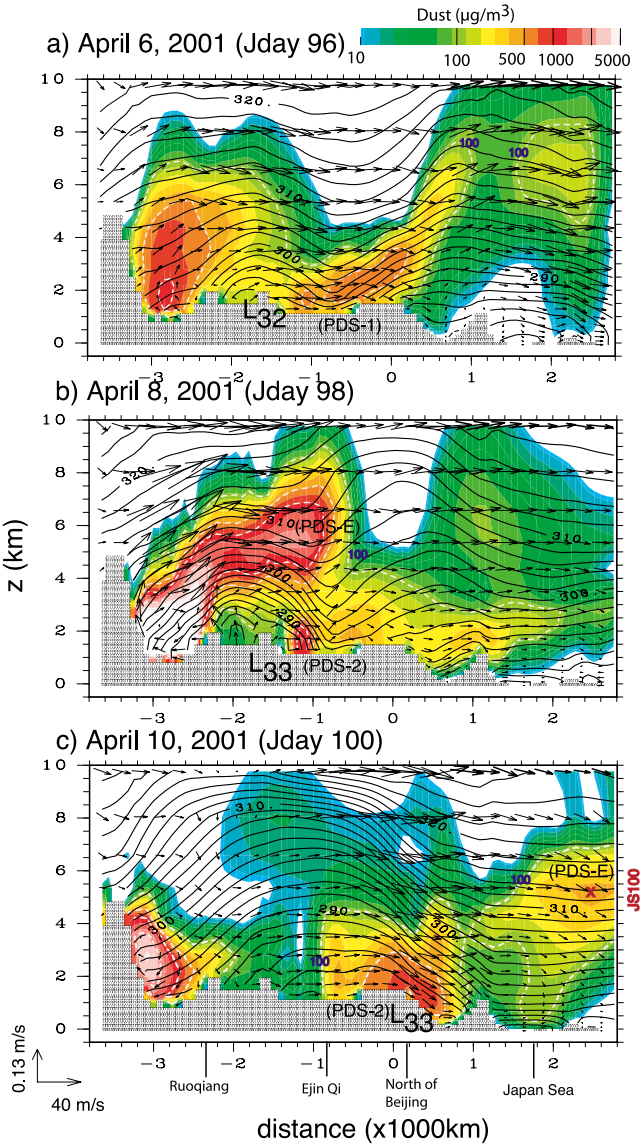

Figure 9. (a–c) Vertical cross section of potential temperature (lines) and dust concentration (color) at Y = 69 (shown in Figure 1) at 0900 JST of each day. L_{32} and L_{33} comprise the low-pressure system shown in Figure 6. Vectors are u and w scaled as shown in wind scale.

parameters, and is a good tool to elucidate the dust structure. Here, we examine the PDS structure in a vertical cross section of dust concentration and a potential temperature field along the west-east line (Y = 69 slice) shown in Figure 1.

[39] Figure 9 shows the vertical cross section of the potential temperature (contour), dust concentration (color), and wind fields (vectors) for 6, 8, and 10 April (Jdays of 96, 98, and 100, respectively) at 0900 JST (0000 UTC). In this figure the terrain following RAMS/CFORS vertical coordinate is transformed to the Cartesian coordinate level, and the stipple region represents the model topography. Horizontal wind vector u and vertical velocity w are plotted in Figure 9 (the vertical scale is enlarged as shown in the wind scale).

[40] On Jday 96 (6 April) (Figure 9a) the low L_{32} (cold air mass) was located in the Gobi region (the area where the potential temperature is below 296 K). A surface dust front was located along this cold front, and the dust plume is shown to penetrate into the upper level (the potential temperature between 290–300 K). This indicates the upper transport of dust into the warm sector. We refer to this feature as PDS-1. This upper dust layer is visible in the lidar measurement data shown in Figure 2a. A sensitivity study without dust emissions from the Gobi shows that the upper portion of PDS-1 is of Taklimakan origin, whereas the lower part of dust is of Gobi origin. Thus PDS-1 consists of a combination of two dust sources. It is important to point out that the averaged potential temperature level over Korea and the Sea of Japan is approximately 280–284 K, which is colder than that of L_{32} cold front (cold air mass). Therefore the main part of the dust cloud in PDS-1 can be transported in elevated layer; also, a fraction of the dust descends into the lower boundary layer.

[41] By Jday 98 (8 April) (Figure 9b) the first dust air mass associated with L_{32} (PDS-1) had already passed over the Beijing region. Its vertical height is below 3 km ASL (at Θ = 296 K). A second cold air mass (L_{33}) is visible between the Taklimakan and Gobi regions. The cold air mass has a potential temperature less than 286 K. The dust layer where Θ = 290 K (PDS-2) is visible at the front of L_{33}. Dust from Taklimakan desert is lifted up in great quantities to the 6 km level (potential temperature between 304–314 K) (PDS-E). This elevated dust layer was generated over the Taklimakan region by extremely strong winds at Jday 97–98 (7–8 April). In these days, a strong wind passed over the Tian Shan Mountains. For example, at Kuqa (82.95°E, 41.72°N), located at the southern foot of Tian Shan Mountains, strong north winds of 19 m/s with 3.6°C temperature (potential temperature of 284.9 K with ww = 35 (severe dust storm)) at Jday of 97.75 (UTC) were reported. A strong east wind (17 m/s, 5.2°C, and ww = 34) that detoured around the high mountains was also reported at Ruoqiang. The condition of these strong winds and vertically weak potential temperature gradient resulted in the lifting of large amounts of dust vertically over the Taklimakan region. Figure 9b clearly shows such vertical lifting processes.

[42] The potential temperature of the BL dust layer is below Θ = 290 K, whereas the highly elevated dust layer is located at Θ = 310 K. Therefore it is possible to distinguish air masses by their potential temperature. Dust uplift is not observed within the warm L_{33} sector. The Θ of this second dust storm is colder than the average Θ level over Korea and the Sea of Japan region, which means that the second dust storm (PDS-2) was produced by cold front activity and penetrated into the lower boundary layer. It is clear that this dust storm not a simple gravity flow or density flow. It is important to point out that some of the dust events are derived from dry line or convective activity. In this paper, we simply use the term "cold-front-derived dust flow," without reference to a specific mechanism.

[43] On Jday 100 (10 April) (Figure 9c) the center of a cold air mass (Θ < 286 K) is located north of Beijing. Most of this dust is trapped within this cold air mass and its vertical dimension was below 4 km (ASL). A strong down draft flow is visible above the cold front, which limits the vertical diffusion and transport of dust. An elevated dust layer (labeled as PDS-E; horizontal scale of 1000 km) is evident over the Sea of Japan (Θ is around 314 K and the dust height is between 4–6 km). This potential temperature

level is consistent with the one simulated in Figure 9b. From this analysis the origin of the elevated dust layer is the Taklimakan desert region.

[44] The vertical motion and horizontal transport of specified air mass can be studied by trajectory analysis. For detailed analysis of PDS, the *Ron Brown* observation path is suitable to understand dust transport during the DS3 episode (see Figure 1). The RAMS-calculated 3-D wind fields (3-hour interval) and Hybrid Particle Transport Model (HYPACT) [*Walko et al.*, 2001] are used to determine air mass trajectories. Note that HYPACT calculation does not assume isentropic motion, but instead uses the RAMS 3-D wind fields directly.

[45] Figure 10a shows the HYPACT backward trajectories. Trajectories of JS100 and RB99 start at z = 5500 m from Jday 100 (10 April) and 99 (9 April), respectively. Trajectories RB102, G102, A102, and MB102 start at z = 550 m above the location of the *Ron Brown* at Jday 100, and from Gosan, Amami, and Mount Bamboo at Jday 102 (12 April), respectively. Open circles along the trajectory path are inserted at 12-hour intervals. Figure 10b shows the time-height cross section of potential temperature (contour) and dust concentration (color) along the *Ron Brown* ship track based on the CFORS model output. Figure 10c compares the observed AOD by *Ron Brown*, CFORS total AOD, and CFORS dust AOD. Figures 10d and 10e show the time-height cross section of dust concentration (color) and potential temperature (contour) along the back trajectories of RB99 and RB102, respectively.

[46] As seen from Figures 10b and 10c, the CFORS dust field (and AOD) shows twin peaks, with an elevated dust layer on Jdays 99–101 and thick boundary layer dust on Jdays 101–102. CFORS predicted AOD capture the observed time variation of AOD. In addition the contribution due to air pollution is approximately 45% of the total AOD when averaged for Jday 96 and 106.

[47] Figure 10d shows the cross section along the back trajectory of this elevated dust layer. The dust belt is shown to be located within the Θ range of 310 and 320 K, with its starting point located over the Taklimakan region. Back trajectories from JS100 and RB99 are almost identical and also have a Taklimakan origin. The transport latitude is near the Y = 69 line shown in Figure 9. Thus the highly elevated dust layer over the Sea of Japan area on Jdays 99–100 is the result of transport from the Taklimakan desert (PDS-E). The boundary layer dense dust shown in Figure 10e arises from the dust onset originated by L_{33} and is transported within the boundary layer as a density flow (because of cold potential temperature level). The dust layer thickness during the transport remains confined in a layer from the surface up to 2 km (where Θ < 290 K).

[48] On the basis of these analyses and Figures 9 and 10 the important sources and transport characteristics of the three dust fractions of the ACE-Asia Perfect Dust Storm (PDS) are identified. The main features are as follows:

[49] 1. The first dust storm (PDS-1) originated from L_{32} and occurred both from the Taklimakan and Gobi regions on Jday 96 (6 April). The potential temperature of this low was warmer than the average Θ level in the coastal region (such as Korea and Japan). The upper part of dust consisted mainly of dust from the Taklimakan region; boundary layer dust was of Gobi origin. The upper layer dust traveled fast

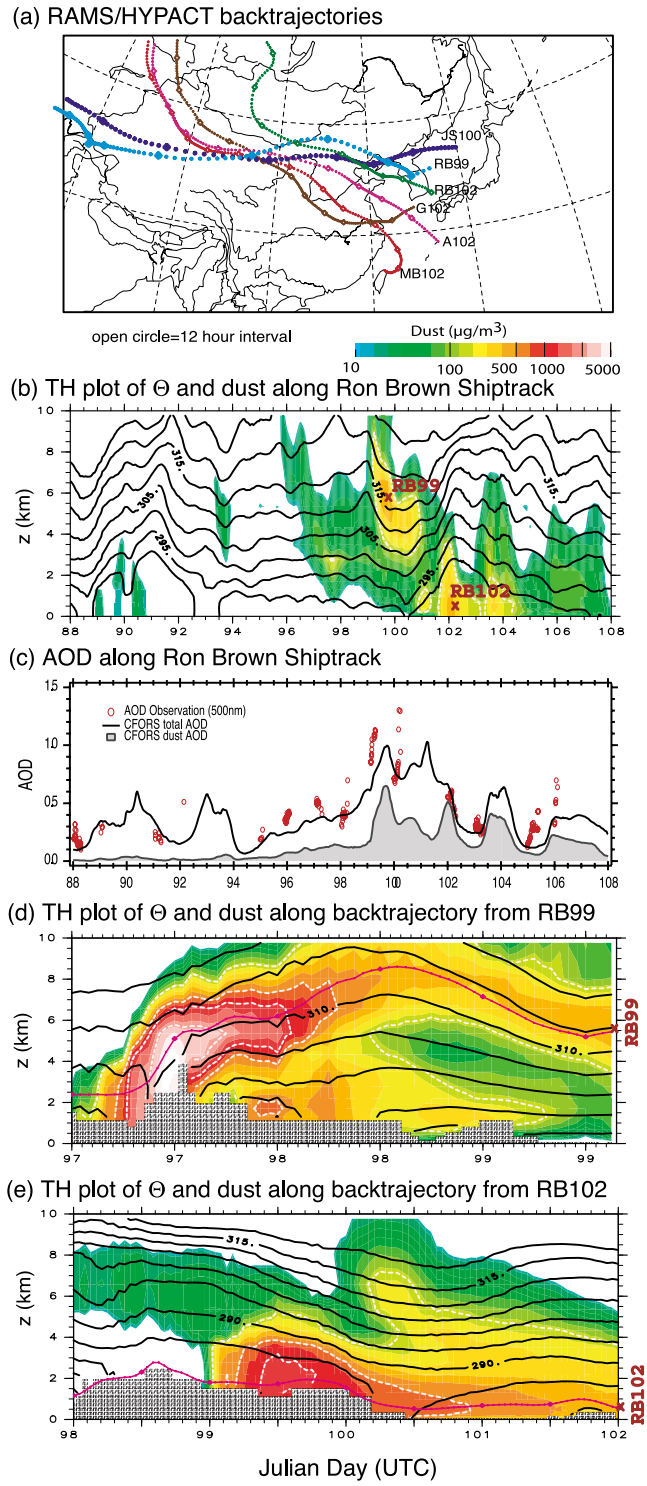

Figure 10. (a) Backward trajectory by HYPACT; (b) time-height cross section of potential temperature (lines) and dust concentration (color) along with the *Ron Brown* ship track; (c) observed AOD on *Ron Brown* (red symbols) and CFORS AOD (lines); (d) as Figure 10b along the trajectory of RB99 shown in Figure 10a starting from z = 5500 m; (e) as Figure 10d, but along trajectory of RB102 and z = 550 m.

within the warm sector. PDS-1 is transported mainly north and did not impact to the lower latitude of model domain.

[50] 2. A second dust storm was associated with L_{33} on Jdays 97–98 (7–8 April). Dust from the Taklimakan region was lifted high by very strong winds up to 5–6 km ASL (Θ ranges 310–320 K). This elevated dust layer had a horizontal area of more than 1000 km and was transported eastward with a height of the Θ of 310–320 K (PDS-E). This PDS-E was observed over the Sea of Japan and wide regions of Japan on Jdays 99–100 (9–10 April).

[51] 3. The main part of the second dust storm (PDS-2) associated with L_{33} originated from the Gobi region on Jdays 98–99 (8–9 April). The temperature of this low was 10°C colder than L_{32}. This dust storm is cold-front-derived dust flow. Its vertical dimension was restricted below 2 km. This cloud split into two parts: One is transported to the north; the other transported to lower latitudes around Taiwan, Okinawa, and Hachijo.

[52] These three dust layers comprise the complicated structure of the ACE-Asia perfect dust storm. The CFORS dust fields clearly explain the detailed PDS structure. This analysis shows that trajectory analysis and potential temperature level analysis are useful tools to analyze the sources and fate of dust storms. Detailed understanding of dust structure is crucial for further analysis of observed and simulated dust concentration.

4.4. Surface Level Dust Onset and Concentration Change: Comparison With Intensive Surface Observation Stations

[53] ACE Asia intensive observations provide a wide range of aerosol observation data [e.g., *Huebert et al.*, 2003]. Here we compare model results with various surface observations taken by the DELTA Group [*Cahill et al.*, 2002], APEX observations by *Nakajima et al.* [2003], and VMAP observations by *Matsumoto et al.* [2003].

[54] The DELTA Group measurements consisted of continuous time- and size-resolved aerosol sampling and elemental analysis that was conducted at six sites during ACE-Asia. Aerosol chemical composition was determined using an eight-stage DRUM aerosol sampling system [*Perry et al.*, 1999]. The DRUM sampler provides size-segregated (0.09–0.26, 0.26–0.34, 0.34–0.56, 0.56–0.75, 0.75–1.15, 1.15–2.5, 2.5–5.0, and 5.0, approximately 12.5 μm in aerodynamic diameter) elemental (sodium through lead) measurements. The DRUM sampler was operated on a continuous cycle with 3-hour resolution. The DRUM aerosol samples were analyzed for inorganics (42 elements between sodium and lead) by synchrotron X-ray fluorescence at the Lawrence Berkeley National Laboratory Advanced Light Source. Averaged analysis error is within 5%.

[55] Variability of Maritime Aerosol Properties (VMAP) [*Matsumoto et al.*, 2003] provided important surface measurements of aerosol composition (elemental and organic carbon, major ions, trace metals and number concentration) and trace gases (SO_2, O_3, CO, and Rn) at four remote islands in Japan. Rishiri and Hachijo islands' observation data were used for comparison. Independent from the VMAP network, surface observations at Amami-Oshima island were conducted under the APEX project [*Nakajima et al.*, 2003]. The sample was connected to a cyclone separator with a 50% cutoff diameter of 2 μm. Daily averaged trace metals, carbonaceous aerosols, and inorganic aerosols were observed at this site. The research vessel *Ron Brown* also provided important observation of aerosol composition over the ocean. Measurement method details and items are reported by *Bates et al.* [2004] and *Quinn et al.* [2004].

[56] These observation sites are shown with blue solid circles in Figure 1. The measurement technique and time resolution differ for each network. Therefore chemical tracers and particle size ranges were selected to elucidate the behavior of typical mineral dusts and anthropogenic pollutants. Coarse aluminum (Al) and calcium (Ca) were used to represent dust, and fine S (SO_4) to reflect anthropogenic pollutants. The potential temperature level at each site was used to understand the change of air masses. Table 1 shows the size ranges of measurements.

[57] Figure 11 shows the time variation of observed and modeled Al and SO_4 concentrations. The DELTA Group's coarse particle mode Al (stages 1–3 of their data) and fine mode S (which is converted to SO_4 by multiplying by a factor of 3) are plotted for Figure 11: Beijing (Figure 11a), Gosan, Korea (Figure 11b), Hefei, China (Figure 11c), Mount Bamboo, Taiwan (Figure 11d), and Tango, Japan (Figure 11f). Figure 11b the observations obtained at Rishiri Island by the VMAP network. Daily averaged coarse Al and fine nss-SO_4 (cutoff diameter of 2.5 μm) are plotted. Figure 11g shows the observation of APEX at Amami-Oshima. The daily averaged coarse mode Al and fine SO_4 are shown. Finally, Figure 11h shows the observations of coarse Al and fine nss-SO_4 measured on board the NOAA research vessel *Ron Brown*. Table 1 provides detailed information regarding the observation sites.

[58] The CFORS model results of coarse dust and SO_4 concentration are also plotted in Figure 11. The green dotted line in the figure also shows the potential temperature level at 950 m obtained from the RAMS meteorological field. Here coarse mode dust concentrations with diameter between 1 and 12.5 μm are extracted from the model dust size bins. Coarse dust and SO_4 concentration are averaged between the model vertical layers 2–4 (surface to 400 m height). For comparison with the *Ron Brown* measurements the model results were extracted along the ship track path (concentration data are in addition averaged from surface to 400 m level). Dust concentrations are plotted on a log scale (except *Ron Brown* (Figure 11h)) to cover the dynamic range of dust concentrations (dust line is not plotted when the concentration becomes smaller than the vertical minimum value).

[59] The DELTA Group measurements started around Jday 80; VMAP and APEX measurements were mainly during April. Therefore the analysis is focused on dust episodes DS2 and DS3. The modeled dust concentrations are shown to agree well with the Al measurements. Agreement of the dust onset times during DS3 is excellent for all sites. Modeled SO_4 concentrations also show good agreement with the measurements. In Beijing, CFORS simulated four peaks in SO_4 between Jdays 90 and 100, which is in good agreement with the fine mode S measurement. As we discussed with the lidar measurements in section 4.2, the first two peaks can be understood by local air pollution. CFORS did not capture these two peaks of Al as they were associated with pollution, and emissions from anthropogenic

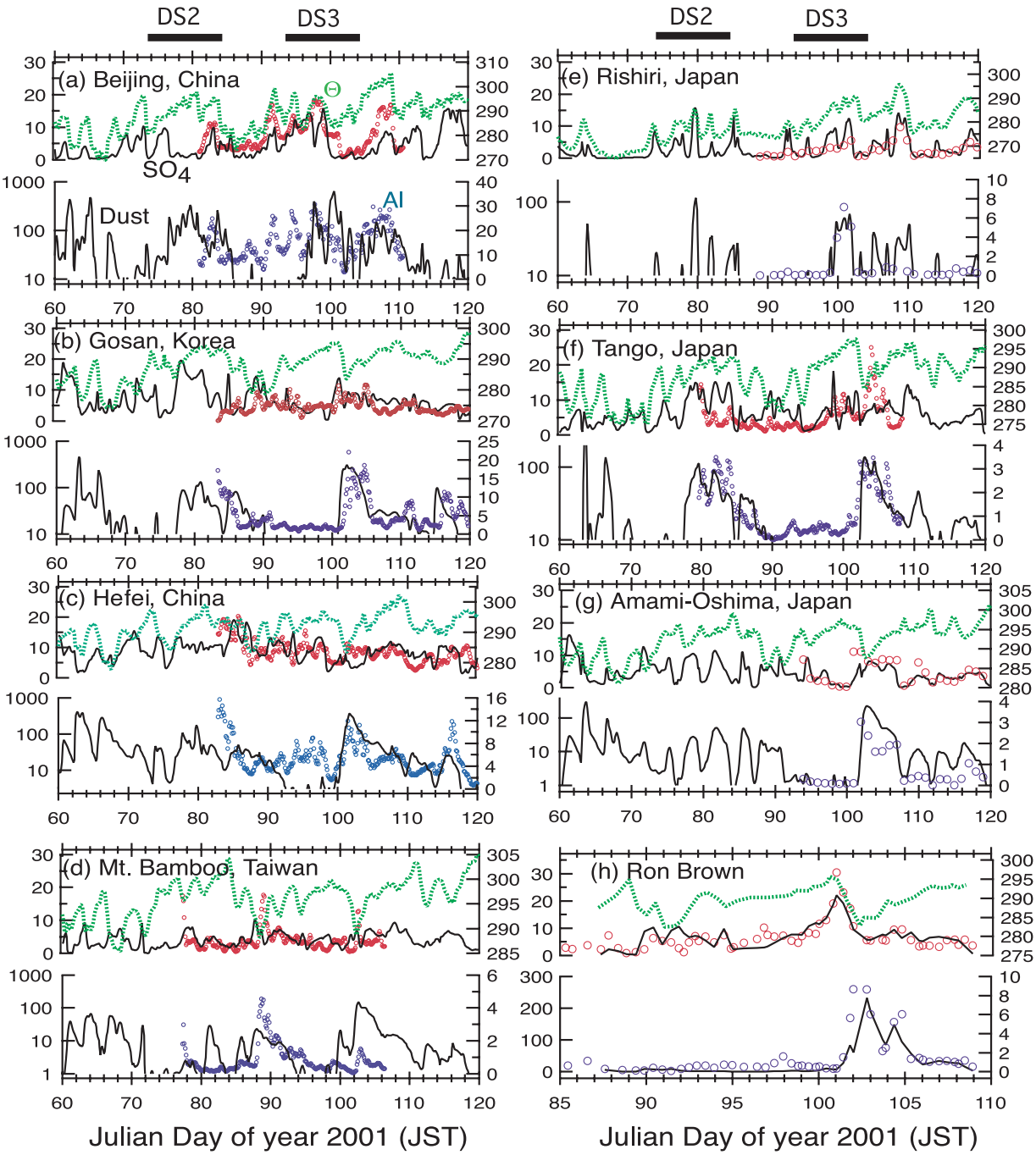

Figure 11. (a–h) Comparison between surface observation and model calculation for SO_4 and coarse mode dust. The red circles show S (or nss-SO_4) observation (left axis with $\mu g/m^3$), and blue circles show coarse Al observation (right axis with $\mu g/m^3$). The green lines show the potential temperature at $z = 950$ m (right axis in K). The black line in the upper part of each panel is CFORS SO_4 (left axis in $\mu g/m^3$). The black line in the lower part of each panel is CFORS coarse mode dust concentration (left axis in $\mu g/m^3$).

dust were not included in the analysis. Note that Al measurements by the DELTA Group are quite consistent with lidar measurements shown in Figure 3.

[60] The time variation of potential temperature provides important information. Except at Beijing and Rishiri, a sudden drop of potential temperature is strongly correlated with the increase of SO_4 and dust. This means that the onset of dust and air pollution was observed with a cold front (cold air mass). Therefore a lag may exist between dust and air pollutants as described by *Uematsu et al.* [2002], but we cannot determine that phenomenon clearly from 4-hour intervals of observation and model output. In Beijing, the approach of a cold front engenders fresh dust storms (without air pollution). It is important to point out that a drop of potential temperature during the DS3 episode for each station is quite consistent ($\Delta\Theta$ is approximately 5–10 K) and can indicate the onset of a cold front. For Rishiri, potential temperature increased with the onset of dust. This

Table 3. Comparison of the Average Concentration During the Typical Dust Episodes

Site and Event	Period, Julian days	Al-Coarse,[a] μg/m^3	Ca-Coarse, μg/m^3	SO_4-Fine, μg/m^3	CFORS Dust-Coarse,[a] μg/m^3	CFORS SO_4, μg/m^3	Al-Coarse/ Dust-CFORS, –	SO_4 (Obs)/(Mdl)
DS2								
Beijing	82.10–86.98	11.91 (0.82)	8.25	5.68	57.02 (0.86)	4.18	0.209	1.36
Gosan	85.021–86.521	6.47 (0.95)	2.65	4.68	72.84 (0.90)	3.43	0.089	1.36
Tango	80.063–84.938	2.41 (0.88)	0.59	4.81	47.77 (0.81)	10.37	0.050	0.46
DS3-1								
Beijing	96.10–98.98	20.44 (0.94)	16.57	14.11	109.34 (0.89)	11.25	0.187	1.254
Rishiri	99.875–101.875	5.34 (0.80)[b]	0.49	4.18	51.49 (0.87)	7.49	0.104	0.558
DS3-2								
Beijing	99.10–101.98	14.58 (0.75)	9.85	6.29	216.40 (0.89)	3.09	0.067	2.036
Gosan	102.021–104.896	14.02 (0.89)	7.57	6.93	186.78 (0.86)	8.19	0.075	0.846
Ron Brown	100.677–104.077	5.17 (0.80)	4.23	10.21	113.82 (0.86)	9.33	0.045	1.094
Hefei	101.104–103.979	8.27 (0.85)	5.74	8.61	194.86 (0.85)	4.29	0.042	2.007
Tango	102.063–106.938	2.45 (0.84)	1.72	9.60	67.94 (0.85)	7.11	0.036	1.350
Amami	101.917–106.917	1.47 (0.71)[c]	–	8.84	96.47 (0.85)	6.52	0.015	1.356
Hachijo	102.875–105.875	2.17 (0.80)[b]	0.87	5.12	73.73 (0.81)	5.92	0.029	0.865
Bamboo	102.063–103.938	0.83 (0.87)	0.30	4.84	106.36 (0.83)	4.87	0.008	0.994
Other events								
Hefei	88.104–90.979	4.13 (0.90)	3.12	8.17	18.73 (0.85)	9.21	0.221	0.887
Bamboo	88.063–90.938	2.86 (0.84)	1.88	8.09	12.09 (0.83)	5.34	0.237	1.515
Beijing	104.10–109.98	20.42 (0.94)	19.24	8.71	66.74 (0.85)	3.86	0.306	2.256
Hefei	114.104–117.979	5.98 (0.92)	2.81	6.26	13.82 (0.83)	8.22	0.433	0.762

[a]Numbers in parentheses shows the coarse fraction.
[b]The $d < 2.5$ μm over total concentration.
[c]The $d < 2.0$ μm over total concentration.

is reasonable because the air mass over the Rishiri area differs from that of the Chinese inland region. Air masses arriving at Rishiri often pass over Far Eastern Siberia and Okhotsk. The average potential temperature over Rishiri was 271.9 K (March) and 277.8 K (April); therefore the increase of potential temperature at Rishiri signals a different air mass that includes dust and air pollution.

[61] Table 3 shows the average concentration of observed Al, Ca, S (converted to SO_4), modeled coarse mode dust, and sulfate during dust episodes DS2, DS3, and other interesting periods. The averaging time period is determined by air mass trajectory analysis to identify the major dust air mass. Table 3 includes the coarse fraction of observed Al and modeled dust. It also shows the Al-coarse/dust-model ratio during the same period. Notably, VMAP and APEX station have a different size range for Al-coarse and Al-total concentration as shown in a footnote of Table 3.

[62] Mineral dust contains approximately 6–8% aluminum [e.g., *Zhang et al.*, 2003]. The Al/Dust ratio ranged from 0.19–0.31 in Beijing (except DS3-2 case). This high ratio reflects the effects of local dust sources around Beijing, which cannot be well simulated by the regional-scale dust model. Similar high Al/dust ratios were also found in Hefei (0.221–0.433) and Mount Bamboo (0.237).

[63] During DS3-2 the Al/dust ratios at Beijing and Gosan were approximately 0.07, and 0.04 for the *Ron Brown*, Hefei, and Tango. Amami, Hachijo and Mount Bamboo showed values on the order of 0.01–0.03. The coarse fraction of Al ranged from 0.75–0.89 at the DELTA Group sites, and did not change systematically with the downwind distance. The calculated ratio of Al/dust tends to decrease when the air mass is transported to the south (lower latitude), whereas the coarse fraction of model dust ranges from 0.81 to 0.89. One key issue is why the CFORS model cannot predict dust concentration well at Amami, Hachijo, and Mount Bamboo for DS3-2 (it is overpredicted)? One reason is the accuracy of the RAMS precipitation amount and CFORS dust wet scavenging parameterization. Precipitation amount at lower latitude (≈30°N) during the March and April 2001 was exceeding 200 mm (see Figure 1 of *Uno et al.* [2003b]) and RAMS precipitation amount has a lower bias. Another important point is that CFORS does not include the in-cloud scavenging processes for dust removal. The importance of wet scavenging is clearly pointed out by *Zhao et al.* [2003]. This comparison indicates that re-examination of wet scavenging is the next issue for CFORS model improvement.

[64] It is interesting that the increase timing of dust and Al at Mount Bamboo is well simulated, but the ratio of Al and dust is completely independent at each dust onset. Detailed analysis of the ratio between the observed Al and calculated dust for each case is very important and more careful examination to elucidate why the ratio is different in Mount Bamboo is an issue for advancing the development of this model.

4.5. Horizontal Dust Transport Flux at 130°E During the Dust Episodes

[65] The transport dust flux at 130°E longitude is interesting for evaluating the importance of Chinese outflow of dust to Korea, Japan, and the Pacific Ocean. The mean cross sections of the longitudinal dust transport fluxes from the west to east across longitude 130°E for each dust episode (DS1, DS2, and DS3) are shown in Figure 12. That figure also includes the average dust concentration by contour line. The averaging period (shown in Figure 12) is selected to include the major part of dust transport for each dust episode (which is different determined in section 3).

[66] Horizontal dust transport fluxes are highest in the Chinese desert regions because dusts are emitted into the atmosphere by high surface winds [*Satake et al.*, 2004]. The general export pathway for dust passing through 130°E can be understood between 35°N and 45°N in westerly flow.

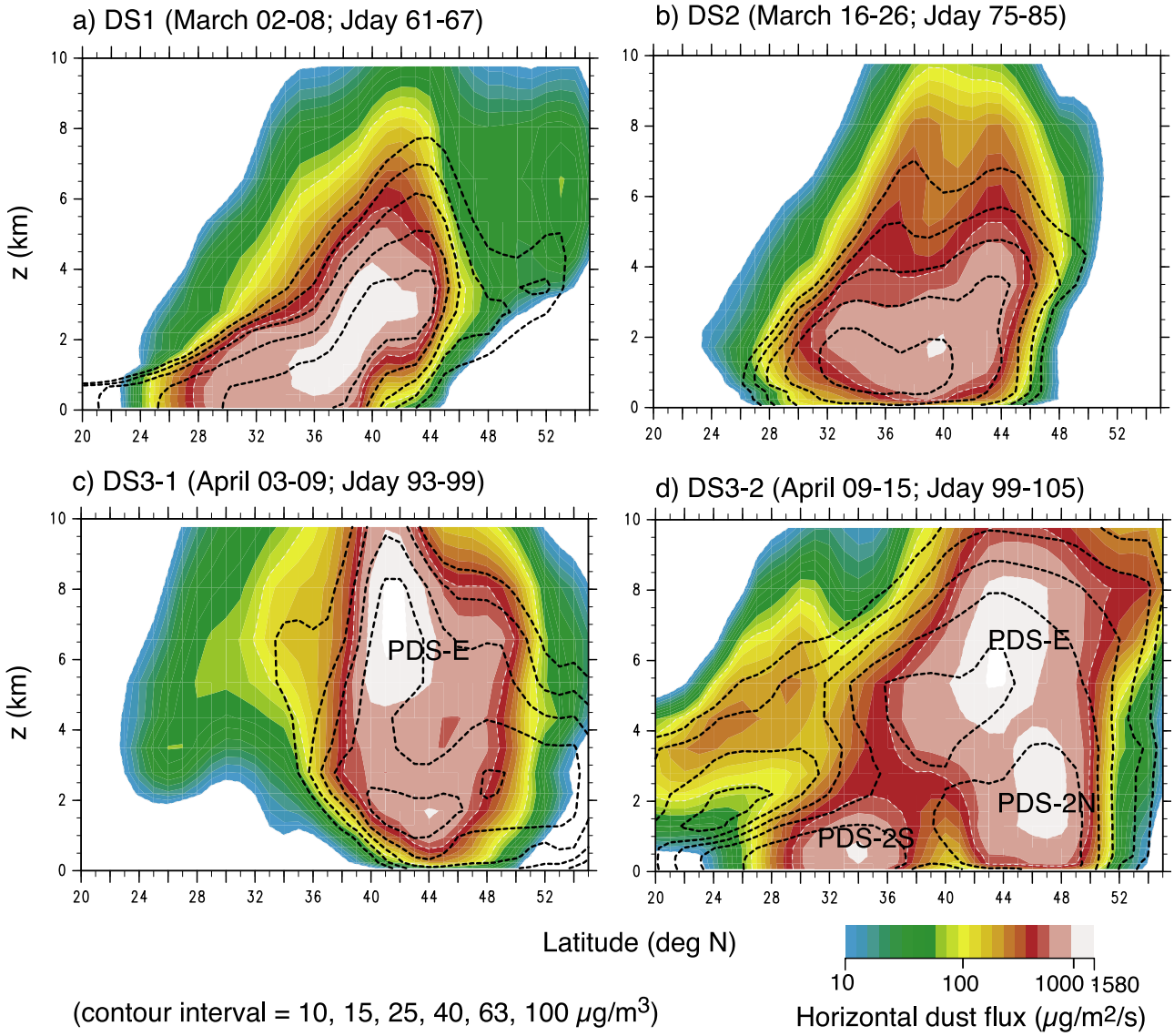

Figure 12. (a–d) Average dust concentration (lines) and horizontal dust transport flux (contour) averaged over the dust episodes along 130°E longitude.

[67] During the DS1, main dust flux is located between 35°N and 42°N, which is elevated from 1–4 km. We can see the southern edge of dust transport flux reached to the latitude of 30°N. The transport pattern in DS2 is different from DS1, one reason is that the main trajectory of the low-pressure system does not come down below 40°N, as discussed in section 3. We can see that the structure of DS3-1 and DS3-2 is quite different. In DS3-1, major dust transport pathway is located in high latitude (between 40°N and 45°N). The elevated dust transport flux is related to the first part of PDS-E (as shown in Figures 9 and 10). In DS3-2, lower latitude dust transport flux is located at 30°N and 36°N, which is the southern branch of PDS-2. Northern dust transport flux located between 46°N and 50°N elevated 1–4 km is another branch of PDS-2. We can also see the highly elevated dust transport flux at 6 km is the PDS-E. Such a complicated structure of dust transport flux is important for detailed understanding of dust outflow from mainland China.

[68] Total amount of transported dust through the 130°E was evaluated. The amounts (fraction from total flux) are 7.9 Tg (14.3%), 10.9 Tg (19.7%), 6.1 Tg (11.1%), and 12.5 Tg (22.7%) for DS1, DS2, DS3-1, and DS3-2, respectively. Overall dust transport flux during March and April is evaluated as 55.2 Tg. The dust transport has a strongly intermittent quality because of cold front activities. Approximately 34% of total dust transport occurred during the DS3 episode. It is notable that 67.8% of dust during March and April 2001 occurred during the selected three dust episode periods.

5. Conclusions

[69] The CFORS chemical transport model was used to analyze detailed dust emission and transport processes during the ACE-Asia intensive observation. Dust modeling results were examined during three major dust episodes (DS1 for Jdays 61–66, DS2 for Jdays

77–84, and DS3 for Jdays 94–104). We found the following:

[70] 1. CFORS wind field and surface dust concentrations at the source region showed good agreement with SYNOP wind speed and dust reports. Modeled dust loading correlates well with TOMS AI; dust loading is transported with the meandering of the synoptic-scale temperature field at 500 hPa. Intensive surface observation data of coarse Al, coarse Ca, and fine mode S (or sulfate) were compared and found that the time variation of CFORS dust field showed the correct onset timing of dust for each observation site.

[71] 2. Detailed examination by time height cross section showed that the CFORS model results captured major dust onsets and vertical structure well. It was confirmed that dust transport was trapped within the typical potential temperature ranges. Quantitative examination of aerosol optical depth by lidar and the model shows that model results agreed within 20% of difference for major dust episodes.

[72] 3. Structure of the ACE-Asia Perfect Dust Storms (PDSs) was clarified by model analysis. It consists of two boundary layer (BL) dust layer and one elevated dust layer (caused by two large low-pressure system movements). This elevated dust layer was originated at the Taklimakan desert area on 7–8 April and transported to the Sea of Japan on 9–10 April.

[73] 4. Overall dust transport flux at 130°E longitude during March and April was evaluated to 55.2 Tg. It shows that the 68% of dust during March–April 2001 occurred during the selected three dust episode periods.

[74] The major conclusions from this study qualitatively agreed with the previous works by *Liu et al.* [2003] and *Gong et al.* [2003]. However, the estimated vertical dust flux and elevated dust concentration level between the present study (e.g., 105 Tg of vertical flux for March and April) and others (640 Tg for 16 days by *Liu et al.* [2003]; 250 Tg for March–May by *Gong et al.* [2003]) are different. One of the reasons of these differences are mainly coming from the surface wind speed which is sensitive to model resolution, the uncertainty of surface land use/soil texture information for the specification of dust emission area, dust removal scheme by dry/wet deposition and complexity of dust emission scheme. These dust emission/transport modeling results during the ACE-Asia indicates the necessity of a kind of dust model intercomparison work to establish more complete dust emission/transport model development for the Asian region.

[75] **Acknowledgments.** This work was partly supported by Research and Development Applying Advanced Computational Science and Technology (ACT-JST) and Core Research for Evolution Science and Technology (CREST) of Japan Science and Technology Corporation (JST). This work (G. R. Carmichael and Y. Tang) was supported in part by grants from the NSF Atmospheric Chemistry Program, NASA ACMAP and GTS programs, and NOAA Global Change Program. Zifa Wang is supported by the "100-talent project of CAS: Impacts of dust storm transport on the environment and climate." AERONET observation data at Beijing were provided by Brent N. Holben of NASA GSFC. This research is a contribution to the International Global Atmospheric Chemistry (IGAC) Core Project of the International Geosphere Biosphere Program (IGBP) and is part of the IGAC Aerosol Characterization Experiments (ACE).

References

Bates, T. S., et al. (2004), Marine boundary layer dust and pollutant transport associated with the passage of a frontal system over eastern Asia, *J. Geophys. Res.*, *109*, D19S19, doi:10.1029/2003JD004094, in press.

Cahill, T. A., S. S. Cliff, M. Jimenez-Cruz, and K. D. Perry (2002), Comparison of two dust storms during ACE-Asia, March and April, 2001, by site, size, time, and composition, paper presented at 6th International Aerosol Conference, Int. Aerosol Res. Assem., Taipei, Taiwan.

Chin, M., P. Ginoux, R. Lucchesi, B. Huebert, R. Weber, T. Anderson, S. Masonis, B. Blomquist, A. Bandy, and D. Thornton (2003), A global aerosol model forecast for the ACE-Asia field experiment, *J. Geophys. Res.*, *108*(D23), 8654, doi:10.1029/2003JD003642.

Conant, W. C., J. H. Seinfeld, J. Wang, G. R. Carmichael, Y. Tang, I. Uno, P. J. Flatau, K. M. Markowicz, and P. K. Quinn (2003), A model for the radiative forcing during ACE-Asia derived from CIRPAS Twin Otter and R/V *Ronald H. Brown* data and comparison with observations, *J. Geophys. Res.*, *108*(D23), 8661, doi:10.1029/2002JD003260.

Cotton, W. R., et al. (2003), RAMS 2001: Current status and future directions, *Meteorol. Atmos. Phys.*, *82*, 5–29.

Fernald, F. G. (1984), Analysis of atmospheric lidar observations: Some comments, *Appl. Opt.*, *23*, 652–653.

Fujita, S., T. Sakurai, and K. Matsuda (2003), Wet and dry deposition of sulfur associated with the eruption of Miyakejima volcano, Japan, *J. Geophys. Res.*, *108*(D15), 4444, doi:10.1029/2002JD003064.

Gillette, D., and R. Passi (1988), Modeling dust emission caused by wind erosion, *J. Geophys. Res.*, *93*, 14,233–14,242.

Gong, S. L., X. Y. Zhang, T. L. Zhao, I. G. McKendry, D. A. Jaffe, and N. M. Lu (2003), Characterization of soil dust aerosol in China and its transport and distribution during 2001 ACE-Asia: 2. Model simulation and validation, *J. Geophys. Res.*, *108*(D9), 4262, doi:10.1029/2002JD002633.

Huebert, B. J., T. Bates, P. B. Russell, G. Shi, Y. J. Kim, K. Kawamura, G. Carmichael, and T. Nakajima (2003), An overview of ACE-Asia: Strategies for quantifying the relationships between Asian aerosols and their climatic impacts, *J. Geophys. Res.*, *108*(D23), 8633, doi:10.1029/2003JD003550.

Intergovernmental Panel on Climate Change (IPCC) (2001), *Climate Change 2001: The Scientific Basis*, edited by J. T. Houghton et al., 896 pp., Cambridge Univ. Press, New York.

Kurosaki, Y., and M. Mikami (2003), Recent frequent dust events and their relation to surface wind in east Asia, *Geophys. Res. Lett.*, *30*(14), 1736, doi:10.1029/2003GL017261.

Liu, M., D. L. Westphal, S. Wang, A. Shimizu, N. Sugimoto, J. Zhou, and Y. Chen (2003), A high-resolution numerical study of the Asian dust storms on April 2001, *J. Geophys. Res.*, *108*(D23), 8653, doi:10.1029/2002JD003178.

Matsumoto, K., M. Uematsu, T. Hayano, K. Yoshioka, H. Tanimoto, and T. Iida (2003), Simultaneous measurements of particulate elemental carbon on the ground observation network over the western North Pacific during the ACE-Asia campaign, *J. Geophys. Res.*, *108*(D23), 8635, doi:10.1029/2002JD002744.

Nakajima, T., et al. (2003), Significance of direct and indirect radiative forcings of aerosols in the East China Sea region, *J. Geophys. Res.*, *108*(D23), 8658, doi:10.1029/2002JD003261.

Nickovic, S., G. Kallos, A. Papadopoulos, and O. Kalaliagou (2001), A model for prediction of desert dust cycle in the atmosphere, *J. Geophys. Res.*, *106*, 18,113–18,129.

Park, S.-U., and H.-J. In (2003), Parameterization of dust emission for the simulation of the yellow sand (Asian dust) event observed in March 2002 in Korea, *J. Geophys. Res.*, *108*(D19), 4618, doi:10.1029/2003JD003484.

Perry, K. D., T. A. Cahill, R. C. Schnell, and J. M. Harris (1999), Long-range transport of anthropogenic aerosols to the NOAA baseline station at Mauna Loa Observatory, Hawaii, *J. Geophys. Res.*, *104*, 18,521–18,533.

Pielke, R. A., et al. (1992), A comprehensive meteorological modeling system: RAMS, *Meteorol. Atmos. Phys.*, *49*, 69–91.

Quinn, P. K., et al. (2004), Aerosol optical properties measured on board the *Ronald H. Brown* during ACE-Asia as a function of aerosol chemical composition and source region, *J. Geophys. Res.*, *109*, D19S01, doi:10.1029/2003JD004010, in press.

Satake, S., et al. (2004), Characteristics of Asian aerosol transport simulated with a regional-scale chemical transport model during the ACE-Asia observation, *J. Geophys. Res.*, *109*, D19S22, doi:10.1029/2003JD003997, in press.

Seinfeld, J. H., et al. (2004), Regional climatic and atmospheric chemical effects of Asian dust and pollution, *Bull. Am. Meteorol. Soc.*, *85*, 367–380.

Shao, Y., E. Jung, and L. M. Leslie (2002), Numerical prediction of northeast Asian dust storms using an integrated wind erosion modeling system, *J. Geophys. Res.*, *107*(D24), 4814, doi:10.1029/2001JD001493.

Shimizu, A., N. Sugimoto, I. Matsui, K. Arao, I. Uno, T. Murayama, N. Kagawa, K. Aoki, A. Uchiyama, and A. Yamazaki (2004), Continuous observations of Asian dust and other aerosols by polarization lidars in

China and Japan during ACE-Asia, *J. Geophys. Res.*, *109*, D19S17, doi:10.1029/2002JD003253.

Sugimoto, N., I. Matsui, A. Shimizu, I. Uno, K. Asai, T. Endoh, and T. Nakajima (2002), Observation of dust and anthropogenic aerosol plumes in the Northwest Pacific with a two-wavelength polarization lidar on board the research vessel *Mirai*, *Geophys. Res. Lett.*, *29*(19), 1901, doi:10.1029/2002GL015112.

Takemura, T., H. Okamoto, Y. Maruyama, A. Numaguti, A. Higurashi, and T. Nakajima (2000), Global three-dimensional simulation of aerosol optical thickness distribution of various origins, *J. Geophys. Res.*, *105*, 17,853–17,873.

Tang, Y., et al. (2004), Impacts of dust on regional tropospheric chemistry during the ACE-Asia experiment: A model study with observations, *J. Geophys. Res.*, *109*, D19S21, doi:10.1029/2003JD003806, in press.

Uematsu, M., A. Yoshikawa, H. Muraki, K. Arao, and I. Uno (2002), Transport of mineral and anthropogenic aerosols during a kosa event over east Asia, *J. Geophys. Res.*, *107*(D7), 4059, doi:10.1029/2001JD000333.

Uno, I., H. Amano, S. Emori, K. Kinoshita, I. Matsui, and N. Sugimoto (2001), Trans-Pacific yellow sand transport observed in April 1998: Numerical simulation, *J. Geophys. Res.*, *106*, 18,331–18,344.

Uno, I., et al. (2003a), Regional chemical weather forecasting system CFORS: Model descriptions and analysis of surface observations at Japanese island stations during the ACE-Asia experiment, *J. Geophys. Res.*, *108*(D23), 8668, doi:10.1029/2002JD002845.

Uno, I., G. R. Carmichael, D. Streets, S. Satake, T. Takemura, J.-H. Woo, M. Uematsu, and S. Ohta (2003b), Analysis of surface black carbon distributions during ACE-Asia using a regional-scale aerosol model, *J. Geophys. Res.*, *108*(D23), 8636, doi:10.1029/2002JD003252.

Walko, R. L., C. J. Tremback, and M. J. Bell (2001), HYPACT: Hybrid Particle and Concentration Transport Model user's guide, ASTER Div., Mission Res. Corp., Santa Barbara, Calif.

Zender, C. S., H. Bian, and D. Newman (2003), Mineral Dust Entrainment and Deposition (DEAD) model: Description and 1990s dust climatology, *J. Geophys. Res.*, *108*(D14), 4416, doi:10.1029/2002JD002775.

Zhang, X. Y., S. L. Gong, Z. X. Shen, F. M. Mei, X. X. Xi, L. C. Liu, Z. J. Zhou, D. Wang, Y. Q. Wang, and Y. Cheng (2003), Characterization of soil dust aerosol in China and its transport and distribution during 2001 ACE-Asia: 1. Network observations, *J. Geophys. Res.*, *108*(D9), 4261, doi:10.1029/2002JD002632.

Zhao, T., S. Gong, X. Y. Zhang, and I. McKendry (2003), Modeled size-segregated wet and dry deposition budgets of soil dust aerosol during ACE-Asia, 2001: Implications for trans-Pacific transport, *J. Geophys. Res.*, *108*(D23), 8665, doi:10.1029/2002JD003363.

T. S. Bates and P. K. Quinn, NOAA Pacific Marine Environmental Laboratory, 7600 Sand Point Way, NE, Seattle, WA 98115, USA. (tim.bates@noaa.gov; quinn@pmel.noaa.gov)

T. A. Cahill and S. Cliff, DELTA Group, Chemical Engineering, University of California, Davis, One Shields Avenue, Davis, CA 95626-5294, USA. (tacahill@ucdavis.edu; sscliff@ucdavis.edu)

G. R. Carmichael and Y. Tang, Center for Global and Regional Environmental Research, University of Iowa, Iowa City, IA 52240, USA. (gcarmich@engineering.uiowa.edu; ytang@cgrer.uiowa.edu)

I. Uno, S. Satake, and T. Takemura, Research Institute for Applied Mechanics, Kyushu University, Kasuga Park 6-1, Kasuga 816-8580, Japan. (iuno@riam.kyushu-u.go.jp; satake@riam.kyushu-u.ac.jp; toshi@riam.kyushu-u.ac.jp)

T. Murayama, Faculty of Marine Engineering, Tokyo University of Marine Science and Technology, Tokyo 135-8533, Japan. (murayama@e.kaiyodai.ac.jp)

S. Ohta, Faculty of Engineering, Hokkaido University, Kita 8 Nishi 5, Sapporo 060-8628, Japan. (ohta@eng.hokudai.ac.jp)

A. Shimizu and N. Sugimoto, National Institute for Environmental Studies, Tsukuba, Onogawa 16-2, Ibaraki 305-8506, Japan. (shimizua@nies.go.jp; nsugimot@nies.go.jp)

M. Uematsu, Ocean Research Institute, University of Tokyo, Nakano-ku, Tokyo 164-8639, Japan. (uematsu@ori.u-tokyo.ac.jp)

Z. Wang, Institute of Atmospheric Physics, CAS, Beijing 100029, China. (zifawang@mail.iap.ac.cn)